

A *Pseudomonas aeruginosa* quorum-sensing inducer controls lung permeability in establishing chronic infection via EGFR

Received: 3 March 2025

Accepted: 17 November 2025

Published online: 09 December 2025

 Check for updatesMingke Zheng^{1,4}, Jie Chen^{2,4}, Gege Qin^{1,4}, Ze Zhang¹, Di Zhai¹, Hefei Ruan^{1,3}, Tie Xia¹, Tongtao Yue²✉ & Yan Shi¹✉

Pseudomonas aeruginosa is an opportunistic pathogen that can cause severe infections in immunocompromised patients. N-(3-oxo-dodecanoyl) homoserine lactone (3oc12) is a small quorum molecule that is used to communicate between bacterial cells and between bacteria and the host. However, the exact molecular mechanisms of this exchange is not yet fully understood. Here, we present a modality that *P. aeruginosa* uses to finetune the severity of lung infection, where 3oc12 is incorporated into the host cell membrane, causing a marked increase in epidermal growth factor receptor (EGFR) ligand-independent self-dimerization. This ligand-free self-activation leads to epidermal growth factor receptor-signal transducer activator of transcription-3 (EGFR-STAT3) signaling, resulting in higher expression of tight junction proteins. This effect reduces the permeability of lung epithelial barrier, which in turn inhibits the release of *P. aeruginosa* from alveoli into the systemic circulation, and is essential to the establishment of long-term infection. This finding suggests a new, pathogen-autonomous mechanism to describe a tendency of *P. aeruginosa* of maintaining persistent chronic infection.

In pathological infections, the host immune system attempts to completely eradicate pathogens to better protect the host. From the perspective of pathogen, its harm to the host must be delicately controlled. If an infection is excessively virulent, the resulting host mortality would mean the loss of habitat. This scenario likely plays out in many long-term infections, however, our research into how this type of regulation works is currently limited.

Pseudomonas aeruginosa is an opportunistic and common hospital-acquired pathogen, capable of causing a wide array of infections, particularly in those with compromised immune defense^{1–5}. It can colonize patients with cystic fibrosis (CF) and chronic obstructive pulmonary disease (COPD), and is the main cause of morbidity and mortality in these patients⁶. *P. aeruginosa* can cause serious lung epithelial barrier damage, resulting in edema, which limits the gas

exchange^{7,8}. The epithelial barrier breakdown would also permit *P. aeruginosa* to enter the blood circulation to induce bacteremia and sepsis^{9–13}. All those assaults on the host are grave, yet most *P. aeruginosa* infections can last years or even decades long. While the bacterial loads are usually high, this gram-negative infection in the lung leads to relatively mild manifestations compared with other pulmonary bacterial pathogens. Host immune responses are likely the main force in controlling the exacerbation, however, we still do not know whether *P. aeruginosa* possesses its intrinsic capacity to actively facilitate this transition into this long-term and anatomically confined infection.

P. aeruginosa quorum-sensing molecules are used to communicate between bacterial cells. It is a cell-density dependent regulatory system controlling the expression of multiple genes and social behavior¹⁴. One of the best studied quorum sensing systems is N-(3-

¹Department of Basic Medical Sciences, School of Medicine; Tsinghua-Peking Center for Life Sciences; Institute of Immunology, Tsinghua University, Beijing, China. ²Institute of Coastal Environmental Pollution Control, Key Laboratory of Marine Environment and Ecology, Ministry of Education, Ocean University of China, Qingdao, China. ³Institute of Biophysics, Chinese Academy of Sciences, Beijing, China. ⁴These authors contributed equally: Mingke Zheng, Jie Chen, Gege Qin. ✉ e-mail: yuetongtao@ouc.edu.cn; yanshi@mail.tsinghua.edu.cn

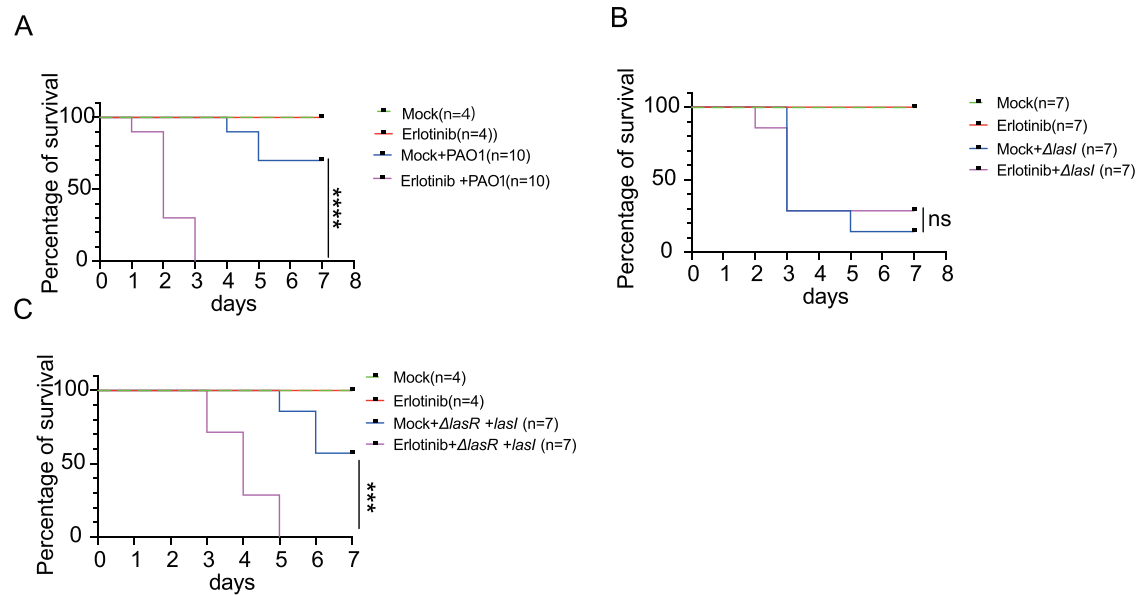


Fig. 1 | The effect of Erlotinib on the survival rate of mice caused by different strains of *P. aeruginosa* infection. A Erlotinib-treated C57BL/6 mice (7 weeks old, male mice, body weight 22 ± 0.5 g) showed higher sensitivity to the wild-type strain *P. aeruginosa* infection. **B** Erlotinib had no effect on the survival rate in *3oc12*-deleted *P. aeruginosa* infection. **C** Survival rate associated with *3oc12* replenished

ΔlasR+lasI strain infection was again reduced with Erlotinib treatment. Kaplan-Meier log-rank was used for survival analysis test. $***P < 0.001$, $****P < 0.0001$, ns: not significant. Graphs are representative of three individual experiments. Source data are provided as a Source Data file.

oxo-dodecanoyl) homoserine lactone (*3oc12*) based on the *LasI/LasR* circuitry in *P. aeruginosa*. *LasI* product *3oc12* regulates a range of events in the community, and its expression is reciprocally controlled by its receptor *LasR*. While *3oc12* is understood as a microbial signaling component, it has widespread effects on host cells. *3oc12* is able to influence lung epithelial cell transcription^{15,16} and binds to IQ motif containing GTPase activating protein 1 (IQGAP1) protein on the cell surface to promote epithelial cell migration¹⁷. *3oc12* has been reported to influence several cell signaling pathways^{18,19} and regulate inflammatory responses^{19–21}. It affects both pro- and anti-inflammatory responses: inhibiting the production of TNF- α , IL-12, and increasing the secretion of IL-6, IL-8, IL-10, and IL-1 β ^{16,22,23}. Some studies have also confirmed that *3oc12* can bind to nuclear peroxisome proliferator-activated receptors (PPARs) to regulate DNA binding activity and nuclear transcription factor- κ B (NF- κ B) signaling pathway-related gene expression²⁴. In particular, *3oc12* has also been reported by us and others of interacting with cholesterol-rich microdomains on lymphocyte cell membranes and influence immune cell signaling^{25,26}.

Several years ago, our lab reported that *3oc12* has a strong affinity for the plasma membrane, its insertion into the membrane causes lipid raft dissolution²⁵. This effect when applied to immune cells causes ligand-independent aggregation of tumor necrosis factor receptor 1 (TNFR1) and its activation. As lung epithelial cells are in direct contact with *P. aeruginosa*, we investigated whether this generalizable effect on lipid rafts would alter other membrane receptor signaling as well. We report here that *3oc12* strongly activated epidermal growth factor receptor (EGFR) on the lung epithelium cells. Here, *3oc12* also caused EGFR ligand-independent activation, and transduced signals via downstream signal transducer activator of transcription-3 (STAT3), resulting in higher expression of several cell tight junction molecules. The loss of this regulation resulted in massive expansion of infected areas and rapid spread of *P. aeruginosa* into the blood circulation. Interestingly, this mechanism can be used in the absence of infection to directly regulate lung permeability for therapeutic purposes. We therefore have potentially identified a simple method employed by *P. aeruginosa* to confine its afflicted area to maintain long term infection. Our work may suggest an intervention method for lung permeability-related diseases.

Results

EGFR is activated in the presence of *3oc12* in *P. aeruginosa* infection

3oc12's effect on the dissolution of lipid rafts is likely universal as lipid-ordered (L_o) and disordered (L_d) domains are present on all mammalian cell membranes^{26,27}. Co-incidentally, EGFR is arguably the most studied transmembrane receptor with reference to lipid order changes²⁸. It has been generally accepted that disruption of lipid rafts induces EGFR activation^{29–31}. Therefore, on the lung epithelial cells, whether *3oc12* regulates EGFR signaling is a valid question. We performed an intranasal administration of WT *P. aeruginosa* (PAO1) as previously reported²⁵ with or without co-injection of Erlotinib, a clinical inhibitor (blocking tyrosine kinase activity, IC₅₀ 20 nM) of the EGFR. This caused a dramatic reduction in survival rate of C57BL/6 mice (Fig. 1A). To rule out any unintended toxicity of Erlotinib, we repeated this experiment with two additional EGFR blockers, PD153035 (IC₅₀ 29 pM) or AG1478 (IC₅₀ 3 nM), the results were the same (Supplementary Fig. 1A). Therefore, EGFR signaling mediates a protective effect during *P. aeruginosa* infection. We next analyzed whether this potential mechanism was mediated by *3oc12*. We have previously generated a *P. aeruginosa* strain with *lasI* deletion ($\Delta lasI$, PAO1 strain with a mutant in *3oc12* encoding region). Infection with this strain caused increased death rate, yet the co-administration of Erlotinib was no longer able to change the mortality (Fig. 1B). This suggested the protective effect of *3oc12* was mediated via EGFR. To confirm the role of EGFR, an $\Delta lasR$ strain with a forced expression (pMMB E67-*lasI* vector) of *3oc12* at comparable levels to that of PAO1 was used ($\Delta lasR + lasI$). As *LasR* is essential to the *LasI/LasR* circuitry, it is not only responsible for the feedback induction of *LasI*, but also mediates several hundred additional events other than *lasI* transcription^{32,33}. In the $\Delta lasR + lasI$ strain, *LasI* is the only mechanism restored with the complete absence of other factors driven by *LasR*²⁵. Here, the mortality associated with this mutant was again sensitive to Erlotinib administration (Fig. 1C). Our data suggested that *3oc12*-mediated membrane disruption caused an EGFR activation event, and this event appeared to be protective of the host in *P. aeruginosa* infection.

Membrane lipid raft disruption causes increased ligand-free dimerization of EGFR

To establish the connection between 3oc12 and EGFR, we used a simplified *in vitro* system. Human lung epithelial cell line A549 was treated with 3oc12 for 20 min, then the lysates were analyzed for levels of phosphorylated EGFR. The result showed that 3oc12 induced EGFR phosphorylation in a dose-dependent manner at tyrosine 1068 site (Fig. 2A). Then we co-cultured supernatants of PAO1, $\Delta lasI$ and $\Delta lasR$ + *lasI* with A549 cells. The data indicated that the presence of 3oc12 was responsible for EGFR phosphorylation (Fig. 2B). Lipid raft removal can increase EGFR diffusion rate on cell membrane in favor of its activation^{31,34}. As endogenously expressed EGFR is difficult to label with precision in a background of uncontrolled noises and nonspecific binding, to track diffusion rate of EGFR on the cell membrane, we used the CRISPR/Cas9 genome-editing tool to produce a knock-in mutant EGFR with a Halo tag attached to the endogenous EGFR in HEK293 cells, and EGFR mobility was tracked with JFX646-HaloTag ligand (Supplementary movies 1–2). Addition of 10 μ M 3oc12 to the knock-in cell line disrupted the lipid raft, partially expelled EGFRs into the disordered lipid phase, and increased the diffusion rate of EGFR (Fig. 2C–G). The model of EGFR motion on living cell membrane can be divided into four patterns: free, confined, directed, immobile^{35,36}, although in this assay the “directed” mode made up less than 0.01% of the total and hence not analyzed. The details in pattern classification are provided in the methods. We found that 3oc12 increased the percentage of free motion pattern and decreased the immobile (Fig. 2D). We also found that the diffusion coefficient of each pattern in 3oc12-treated group was higher than the control group (Fig. 2F). EGFR activation is the result of monomeric EGFR dimerization on the cell surface, in response to its ligand^{37,38}. Again, to avoid the interference from the endogenous receptor, we transfected EGFR-mEGFP plasmid into MCF7 cells, which endogenously express very low level of EGFR, and used single-molecule photobleaching step-counting (SMPSC) to check whether 3oc12 induced EGFR dimer formation on the cell surface^{25,39,40}. The results showed that 3oc12 was indeed able to increase the number of dimers (Fig. 2H). Collectively, these data demonstrated that 3oc12 activated the EGFR on lung epithelial cells, potentially by changing lipid order.

As the cortical cytoskeleton may alter the diffusion coefficient of transmembrane receptors⁴¹, we performed Structured Illumination Microscopy (SIM) to examine the membrane-proximal actin network before and after 3oc12 treatment. We did not find evidence indicating that the addition of 3oc12 directly altered the cortical actin filament and stress fiber structure in HeLa or A549 cells (Fig. 2I and Supplementary Fig. 2A–C), which seems to suggest that in our system 3oc12 does not heavily influence receptor diffusion via blocking their association with the cytoskeleton.

Lipid raft disruption leads to EGFR dimerization

To elucidate the molecular mechanisms of EGFR dimerization influenced by the membrane phase state, we carried out all-atom molecular dynamics (MD) simulations. Two membrane patches of L_o and L_d phase states were employed to represent the intact and disrupted states of lipid rafts, respectively (Supplementary Fig. 3). It is known that phosphatidylinositol(4,5)bisphosphate (PI(4,5)P2) present in the inner leaflet of cell membrane may associate with the juxtamembrane domain of EGFR and inhibit the dimerization^{42,43}. To check whether 3oc12 molecules can penetrate through the membrane and interact with PI(4,5)P2 to impact EGFR dimerization, we prepared a simulation system, where nine 3oc12 molecules were positioned above the membrane with six PI(4,5)P2 molecules randomly distributed in the inner leaflet. After 100 ns unbiased MD simulation, all the 3oc12 molecules successfully inserted into the membrane (Supplementary Fig. 4A). We then calculated the interaction energy between 3oc12 and PI(4,5)P2 (Supplementary Fig. 4B) and found

weak and occasional interactions occurring mostly between the hydrophobic chains of 3oc12 and PI(4,5)P2 (Supplementary Fig. 4C). To further characterize the distribution of 3oc12 across the membrane, we calculated the density distribution of 3oc12 and other membrane components along the membrane normal direction (Supplementary Fig. 4D). These data indicate that 3oc12 molecules are difficult to penetrate through the membrane and form effective interactions with PI(4,5)P2.

With PI(4,5)P2 ruled out, our results showed that in the L_o system, the transmembrane domains of EGFR remained monomeric in the finite simulation period (200 ns) (Fig. 3A). Upon disruption of the lipid raft domain, as indicated by the L_d system, two monomers of EGFR were found to form a dimer shortly via a polar GxxxG-like motif, and the dimer was stable in the last 100 ns (Fig. 3B)⁴⁴. We quantified these observations by examining the proximity of the GxxxG-like motifs. In the L_o system, the distance kept fluctuated around the initial value of 2 nm (Fig. 3C). However, the L_d system displayed a contrasting trend where the distance between two motifs gradually decreased until a minimal value of 0.93 nm was reached (Fig. 3D). This shortest distance was similar to that measured by NMR experiments⁴⁴, suggesting that a stable dimer of EGFR was formed in the non-raft membrane domain. Moreover, the inter-molecular residue contact maps further supported our findings (Fig. 3E, F). Dimerization of the EGFR occurred exclusively in the L_d system, with the interaction sites corresponding to the GxxxG-like motifs (Fig. 3F). Furthermore, through calculating the interaction energy, we discovered that van der Waals interactions played a pivotal role in the EGFR dimerization (Fig. 3G, H). Since our simulation systems mainly adopt four components that constitute the L_o and L_d phase membranes, we further constructed two complex models consisting of more lipid components. We obtained similar results, i.e., EGFR remained monomeric in the L_o phase membrane but rapidly formed dimerization in the L_o system (Supplementary Fig. 5). To further validate our conclusion, we constructed a plasma membrane model with coexisting L_o and L_d phase domains, with five EGFR dimers pre-positioned at the phase boundary. We observed that the EGFR dimers preferred the L_d phase domain and remained there throughout the 4 μ s simulation (Supplementary Fig. 6A). The two-dimensional (2D) radial distribution functions (RDF) further confirmed EGFR dimer accumulation in the L_d phase (Supplementary Fig. 6B). In all, the transmembrane domains of EGFR prefer to be monomeric in the lipid raft domain but immediately dimerize upon disruption of the lipid raft by 3oc12, triggering the ligand-free activation of EGFR. As EGFR has been used as a model for spontaneous activation upon disruption of L_o , via computational biological analysis, we believe our study is the first to propose a motif-based dimerization mechanism that clearly explains EGFR's persistent signaling in domain-less lipid bilayers.

Thermodynamic and kinetic analysis of EGFR dimerization dictated by the membrane phase state

While the MD analysis indicated a strong bias towards self-dimerization of EGFR in L_d domains, we explored further whether such a behavior is supported by changes in the system's free energy. Dimerization of EGFR in the lipid bilayer membrane can induce changes in the enthalpy and entropy of the system. Thus, quantifying the interactions between EGFR and lipids can help elucidate the mechanisms controlling the selective dimerization of EGFR in membranes with different phase states⁴⁵. Compared to the membrane patches rich in unsaturated lipids, lipid rafts are primarily composed of sphingolipids and cholesterol, resulting in a thicker, tighter, and less fluid structure⁴⁶. This feature was characterized by the higher degree of lipid ordering in the L_o system than that in the L_d system (Fig. 4A, C). The presence of EGFR disrupted the normal lipid packing in the L_o system, thus decreasing the order parameter for lipids around EGFR. Dimerization of EGFR induced less contacts with lipids, thus decreasing entropy of

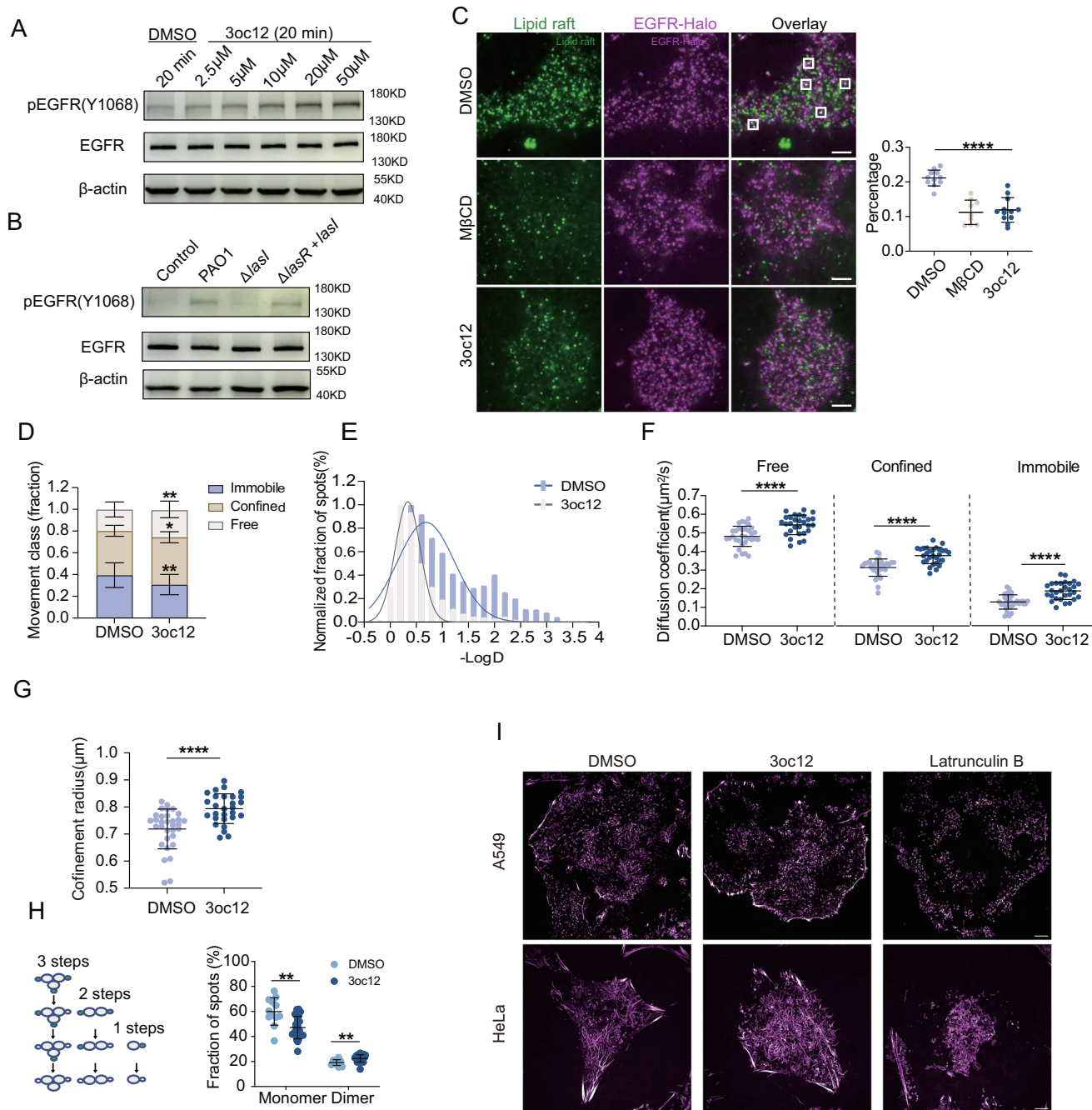


Fig. 2 | Membrane lipid raft disruption causes ligand-free increased dimerization of EGFR. **A** 3oc12-induced EGFR phosphorylation in dose dependent manner.

B Co-cultured supernatants of different strains of *P. aeruginosa* with A549 cells: $\Delta lasI$ strain that lacks the 3oc12 production was less able to induce EGFR phosphorylation. **C** Fluorescently labeled EGFR-Halo (by JFX646-HaloTag ligand) partially colocalizes with Alexa555-conjugated Cholera toxin-B labeled lipid rafts before, but not after, treatment with 10 mM M β CD or 10 μ M 3oc12. Scale bar, 5 μ m. The bottom panel showed the fraction of EGFR-Halo spots in lipid raft structures before and after treatment with M β CD or 3oc12. Data are presented as the mean \pm SD ($n = 11, 9$ and 12 cells). **D** Stacked Histogram shows fractions of EGFR tracks classified as free, confined, or immobile under 3oc12 stimulation. Data are representative of three independent experiments and are presented as the mean \pm SD ($n = 32, 29$). **E** Distributions of the diffusion coefficient of membrane-docked EGFR molecules before and after 3oc12 treatment. **F** The diffusion coefficient values for free, confined, and immobile diffusion states of EGFR molecules

under 3oc12 stimulation. Data are representative of three independent experiments and are presented as the mean \pm SD ($n = 32, 29$). **G** Confinement radius distribution of confined track segments for each condition. Minimal of 1000 trajectories from approximately 30 cells each in DMSO and 3oc12-stimulated groups from three experiments were selected for analysis ($n = 32, 28$). Data represent mean \pm SD.

H SMPS analysis of dimer formation of EGFR-mEGFP on 3oc12-treated cell surface. The results of each group were counted from 10 to 30 cells with more than 4000 individual fluorescent molecules. Data are representative of two independent experiments and are presented as the mean \pm SD ($n = 12, 24, 12, 24$). **I** Super-resolution structured illumination (SIM) imaging of cortical actin filaments using TIRF illumination mode. The representative images of the actin cytoskeleton of cells with DMSO, 3oc12 (10 μ M), or latrunculin B (375 nM) treatment were shown. (**C, D, F, G** and **H**). Statistical significance was tested by two-tailed unpaired Student's *t*-test. * $P < 0.05$, ** $P < 0.01$, **** $P < 0.0001$. Source data are provided as a Source Data file.

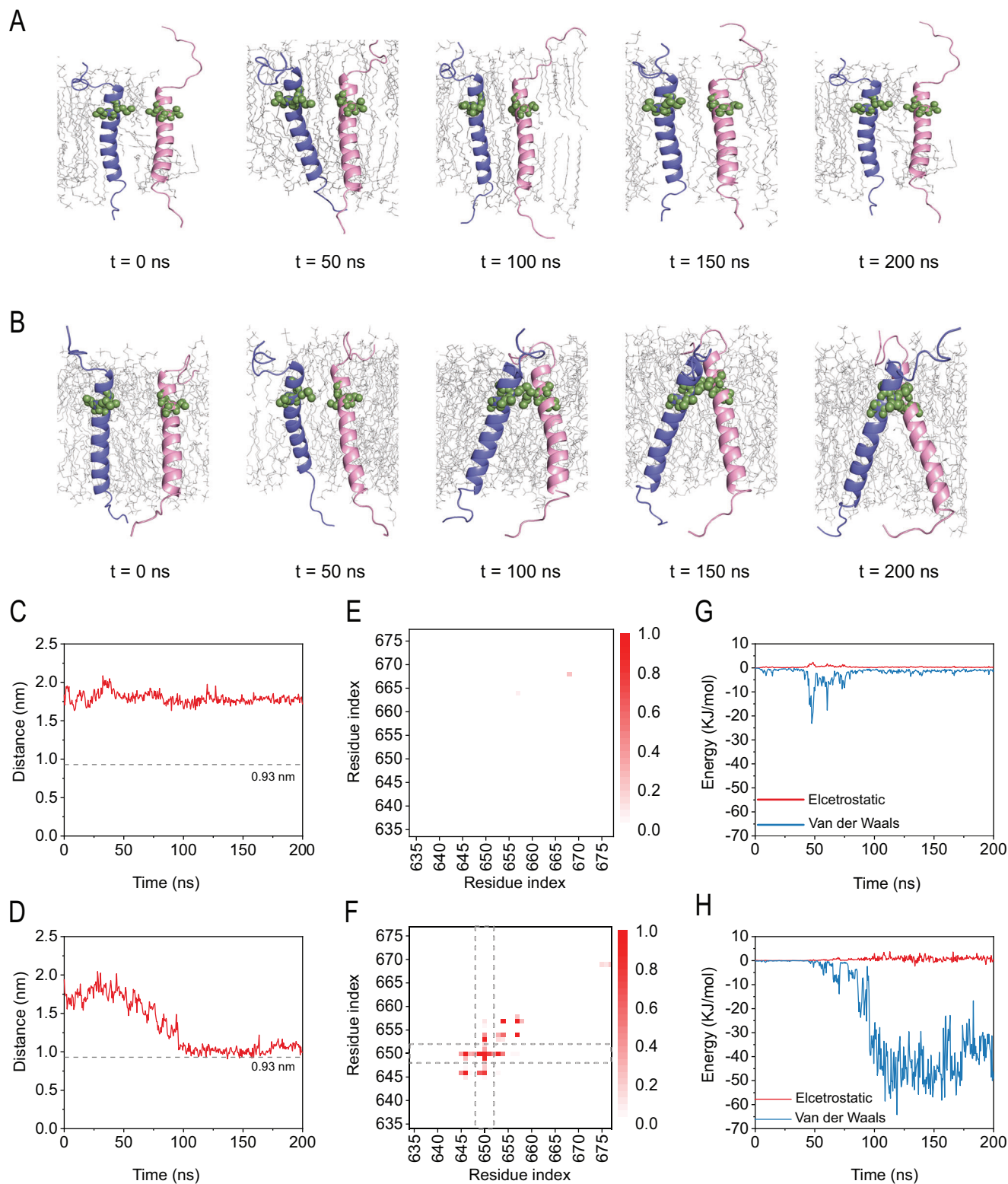


Fig. 3 | Influence of the membrane phase state on EGFR dimerization revealed by all-atoms MD simulations. Time sequences of simulated snapshots depicting the states of two transmembrane domains of EGFR in the L_0 (A) and L_d (B) phase membranes. The GxxxG-like motifs participating in the dimerization are displayed as green beads. C, D Time evolutions of the distance between GxxxG-like motifs of

EGFR in L_0 (C) and L_d (D) phase membranes. Residue contact maps of EGFR in L_0 (E) and L_d (F) phase membranes. The locations of GxxxG-like motifs in dimerized EGFR in the L_d phase membrane were labeled with gray dashed lines. Time evolutions of the van der Waals and electrostatic interaction energies between two monomers in L_0 (G) and L_d (H) phase membranes. Source data are provided as a Source Data file.

the L_0 system (Fig. 4A, B). This decrease in entropy corresponds to increase in the Gibbs free energy, thus being unfavorable to dimerization of EGFR. In contrast, no apparent change in the lipid ordering was observed for EGFR dimerization in the L_d system (Fig. 4C, D). The

transmembrane domain of EGFR tended to tilt in the L_d phase domain due to the positive hydrophobic mismatch. The tilting of EGFR was beneficial for the contacts of GxxxG-like motifs, being responsible for EGFR dimerization (Fig. 3B).

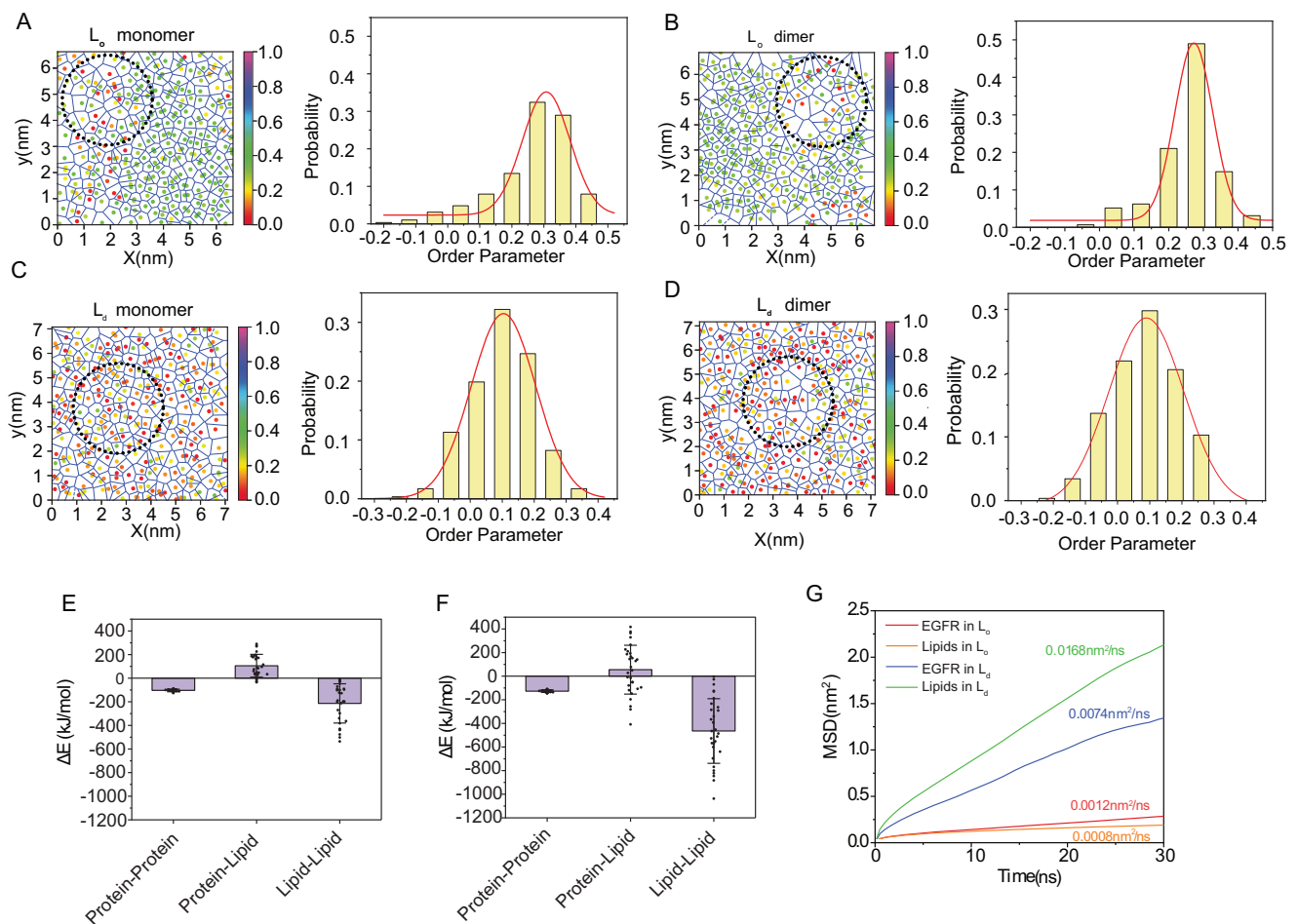


Fig. 4 | Thermodynamic and kinetic analysis of EGFR dimerization in L_o and L_d phase membrane systems. Two transmembrane domains of EGFR in either monomeric or dimeric forms were incorporated in two membranes of L_o and L_d phase states, and each simulation was performed for 200 ns. The lipid order parameter diagrams and the probability distributions when monomeric (A, C) and dimerized (B, D) EGFR were incorporated in the L_o (A, B) and L_d (C, D) phase

membranes. **E** Changes in protein-protein, protein-lipid and lipid-lipid interaction energies after dimerization of EGFR in L_o (E) ($n = 30, 30, 30$) and L_d (F) ($n = 30, 30, 30$) systems. **G** Mean square displacements (MSD) of EGFR and lipids in L_o and L_d systems. The diffusion constants were calculated by fitting the MSD curves and marked aside the lines. Data are as the mean \pm SD. Source data are provided as a Source Data file.

We further calculated the energy of interactions between different components to comparatively analyze the enthalpy change induced by EGFR dimerization in L_o and L_d systems. As shown in Fig. 4E, F, dimerization of EGFR induced decreases of the protein-protein and lipid-lipid interaction energies in both L_o and L_d systems. By contrast, EGFR dimerization in the L_o system induced more increase of the protein-lipid interaction energy than that in the L_d system. It suggested that the dimerization of EGFR in the L_o system was less favorable in enthalpy than that in the L_d system.

In addition to the thermodynamic contribution, the dimerization of EGFR could be influenced by the membrane fluidity. We thus conducted a kinetic analysis on the diffusivity of different components in the L_o and L_d membrane systems. Mean square displacements (MSD) for both EGFR and lipid components were calculated according to the trajectories of MD simulations (Fig. 4G). As expected, the diffusivity of lipids was significantly reduced by forming raft domains. In accordance, the diffusion rate of EGFR in the L_o system was much lower than that in the L_d phase membrane. These results indicated that disruption of lipid rafts can enhance the membrane fluidity to promote the movement of EGFR, creating favorable conditions for dimerization. This result echoed our particle-tracking and SMPSC results.

Overall, our simulation results revealed that the dimerization of EGFR in the lipid raft domain can be both thermodynamically and

kinetically hindered. Upon disruption of the lipid raft to form a L_d phase domain, the EGFR dimerization became thermodynamically favorable and can be accomplished shortly due to the enhanced diffusivity. This suggested that the ligand-free activation of EGFR may be more dependent on its membrane environment rather than the EGFR itself.

Juxtamembrane or the entire extracellular domain of EGFR minimally impacts EGFR dimerization

While the transmembrane domain of EGFR directly senses the membrane change, the extracellular domain of EGFR has been suggested to impede the dimerization of EGFR⁴⁷. In addition, whether the interactions between the juxtamembrane domain and PI(4,5)P2 influence EGFR dimerization remains unknown. We prepared two additional simulation systems to take these two factors into consideration. Our simulations of EGFR with transmembrane and juxtamembrane domains showed that they remained monomeric in the L_o phase, while dimerization occurred in the L_d phase membrane (Fig. 5A, B). The distinct behaviors in response to the membrane phase state were further reflected in the distances between GxxxG-like motifs (Fig. 5C, D), the residue contact maps (Fig. 5E, F), and the interaction energies between transmembrane domains (Fig. 5G). We also calculated the distances between juxtamembrane domains, and it showed an

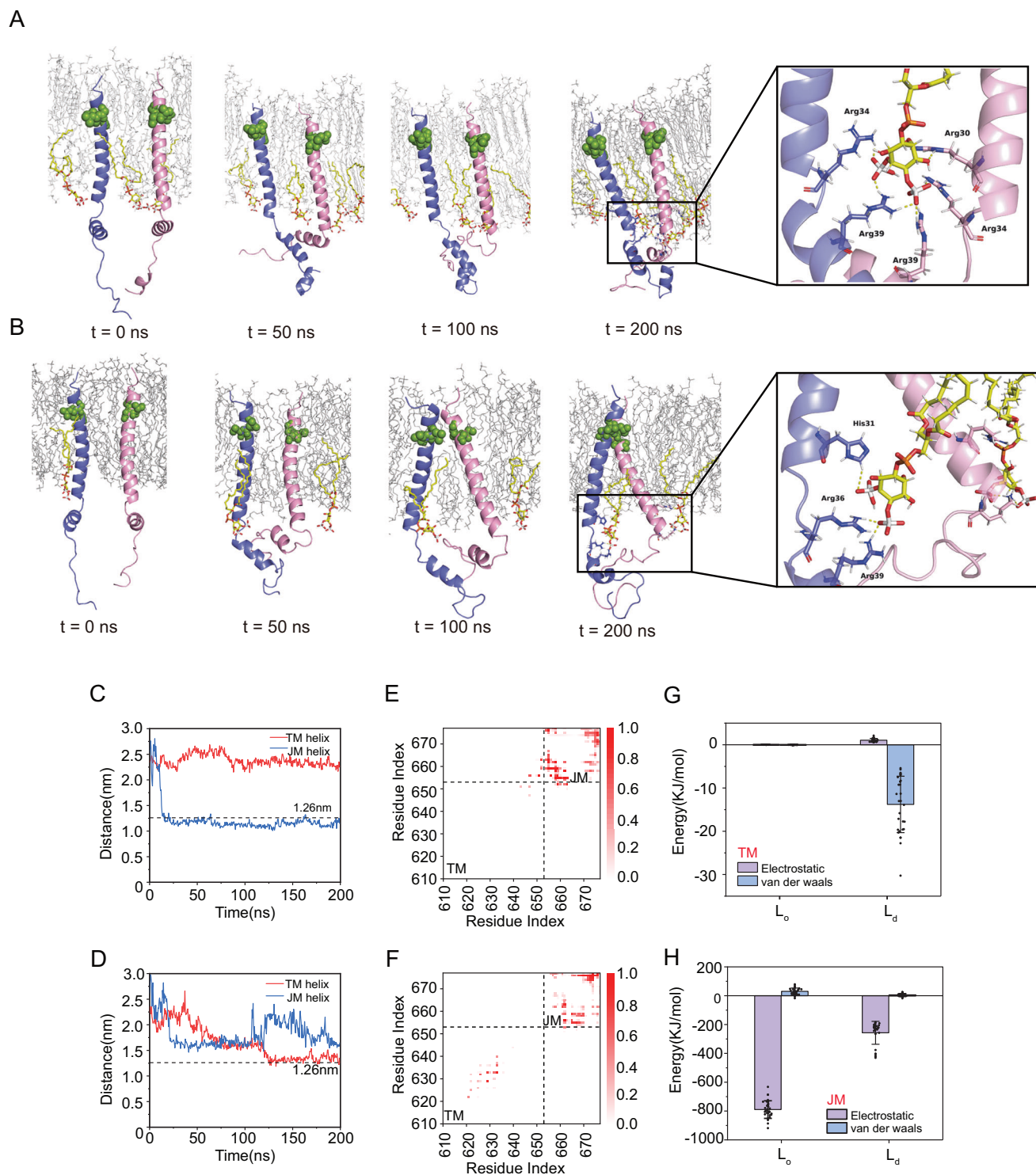


Fig. 5 | Effect of the juxtamembrane domain on EGFR dimerization in L_o and L_d phase membranes with PI(4,5)P2 molecules present in the inner leaflet.

A, B Time sequences of simulated snapshots depicting the states of EGFR containing juxtamembrane and transmembrane domains in the L_o (**A**) and L_d (**B**) phase membranes. The GxxxG-like motifs participating in the dimerization are displayed as green beads. PI(4,5)P2 molecules are displayed in yellow. The right panel of each figure shows an enlarged image illustrating interactions between juxtamembrane domains of EGFR and PI(4,5)P2 in the inner leaflet. Time evolutions of the distance

between GxxxG-like motifs of EGFR in L_o (**C**) and L_d (**D**) phase membranes (red lines). The distances between juxtamembrane domains are also displayed (blue lines). Residue contact maps of EGFR in L_o (**E**) and L_d (**F**) phase membranes. Transmembrane and juxtamembrane domains are separated by dashed lines. Average interaction energies between transmembrane domains (**G**) ($n = 30,30,30,30$) and juxtamembrane domains (**H**) ($n = 30,30,30,30$) of EGFR in L_o and L_d phase membranes. Data are as the mean \pm SD. Source data are provided as a Source Data file.

opposite trend with the transmembrane domain of EGFR in the L_d phase membrane (Fig. 5D). Since the length of the transmembrane domain of EGFR is longer than the membrane thickness, the transmembrane domain tends to tilt. In such a case, the dimerization of

EGFR can be thought as a scissor movement, where the proximity of the transmembrane domain is accompanied by the separation of the juxtamembrane domain. In the L_o phase membrane recruiting more PI(4,5)P2 molecules in the inner leaflet, and more electrostatic

interactions are formed between the juxtamembrane domain and PI(4,5)P₂, and which would be unfavorable to dimerization of the transmembrane domain. In contrast, in the L_d phase, where PI(4,5)P₂ molecules were less concentrated, the interactions between PI(4,5)P₂ and the juxtamembrane domain were considerably reduced (Fig. 5H). This relatively weak interaction did not inhibit dimerization of the transmembrane domain in the L_d phase membrane. Overall, the interactions between the juxtamembrane domain and PI(4,5)P₂ are detrimental to EGFR dimerization, but the response of EGFR to changes in the membrane phase state can overcome this hindrance.

To address the effect of the extracellular domain, we performed MD simulations on EGFR with the complete extracellular and transmembrane domains. Experimental results from photobleaching can only be interpreted as a proximity reading limited by the optical diffraction, rather than the nanometer-scale distance in a true dimer formation. 10 nm is still beyond the limit of the latest super resolution imaging. In this work, we instead used all-atom MD simulations to analyze molecular interactions in GxxG-like motif-dependent EGFR dimerization sensing membrane phase transition from L_o to L_d. Our results showed that the entire EGFR preferred to exist as a monomer in the lipid raft domain but rapidly dimerized upon disruption of the raft domain (Supplementary Fig. 7A, B). The distances, interaction energy and residue contact maps between transmembrane domains all confirmed that dimerization occurred in the L_d system rather than the L_o system (Supplementary Fig. 7C–F). The dimerization of EGFR in the L_d phase membrane was revealed to be thermodynamically and kinetically favorable. Thermodynamically, the changes in entropy and enthalpy indicate the possibility of spontaneous dimerization of EGFR in L_d phase membrane. Dynamically, the diffusivity of both phospholipids and proteins were dramatically increased upon disruption of the lipid raft domain, which is favorable to rapid dimerization (Supplementary Fig. 7G). Therefore, our simulations revealed a motif-based dimerization mechanism that clearly explains the EGFR's persistent signaling in domain-less membrane.

3oc12-EGFR axis protects against dissemination of *P. aeruginosa* infection

To reveal how EGFR signaling provides protection in *P. aeruginosa* infection, we again performed in vivo experiments with or without Erlotinib. In the Bronchoalveolar Lavage Fluid (BALF), the levels of IL-1 α , IL-1 β , IFN- γ , IL-6, and TNF- α showed almost no difference between the PAO1 group and the Erlotinib-treated PAO1 group mice, although IL-1 α , IL-1 β and IFN- γ showed slight increase (Supplementary Fig. 8). Despite the significant contrast in survival rates between the treated and untreated mice, the overall cytokines difference was modest. We then performed *P. aeruginosa* CFU counts in mice lung tissue (Fig. 6A). Surprisingly, the bacterial load was slightly lower in Erlotinib-treated PAO1 mice. Therefore, the higher mortality rate exhibited in the Erlotinib group was not due to intensity of inflammation or bacterial load. We then examined the number of inflammatory infiltrates in the BALF, the total cells and neutrophil counts were significantly higher in the Erlotinib-treated PAO1 group (Fig. 6B, C). Upon visual inspection, the lung of the Erlotinib-treated PAO1 group showed severe hyperemia (Fig. 6D). This seemed to indicate a breach of barrier function in the lung upon EGFR inhibition. H&E staining results showed that the Erlotinib-treated PAO1 group lungs had more immune cells infiltration and epithelial barrier disruption (Fig. 6E), which confirmed the elevated cells counts in the BALF. Tissue damage is accompanied by repair, especially the differentiation of AT2 cells and stem cells into AT1 cells⁴⁸. We stained the lung tissue for Ki67 (cell cycle marker), the result showed that there were more Ki67⁺ cells in the Erlotinib-treated PAO1 group (Fig. 6F), echoing a more active repair upon greater damage in the epithelial barrier. Lung epithelial barrier injury results in large amount of water and proteins entering the respiratory tract. We used Micro-CT to check the pathological changes of lung tissue. The

Mock+PAO1 group mice showed typical infection pathology: the lung tissue displayed frosted glass pathology with fuzzy edges and fluid exudation inside the tissue. However, the Erlotinib-treated PAO1 group mice had more severe lung lesions, unclear tissue interface, obvious destruction of gas-liquid interface, and presented purulent lesion (Fig. 6G). In addition, the BALF protein level was increased in the Erlotinib-treated PAO1 group (Fig. 6H), and the dry/wet ratio of lung tissue (a reverse indicator of lung permeability) decreased significantly after EGFR inhibition (Fig. 6I). We also checked the concentration of arachidonic acid in the BALF, a marker associated with permeability of local blood vessels at the site of inflammation. Again, the result was higher in the Erlotinib-treated PAO1 group (Fig. 6J). *P. aeruginosa* can transmigrate through the pulmonary epithelial barrier into the blood and reach distal organs when the epithelial barrier is damaged. We checked IL-6 concentrations in serum as well as the CFU in spleen and liver. The group of the Erlotinib-treated PAO1 group had higher concentrations of IL-6 in serum and more bacterial load in distal organs (liver and spleen) (Fig. 6K–M). All these data suggested that during *P. aeruginosa* lung infection, EGFR signaling was to reduce the local permeability, a mechanism potentially exploited by *P. aeruginosa* via 3oc12 for its shielding.

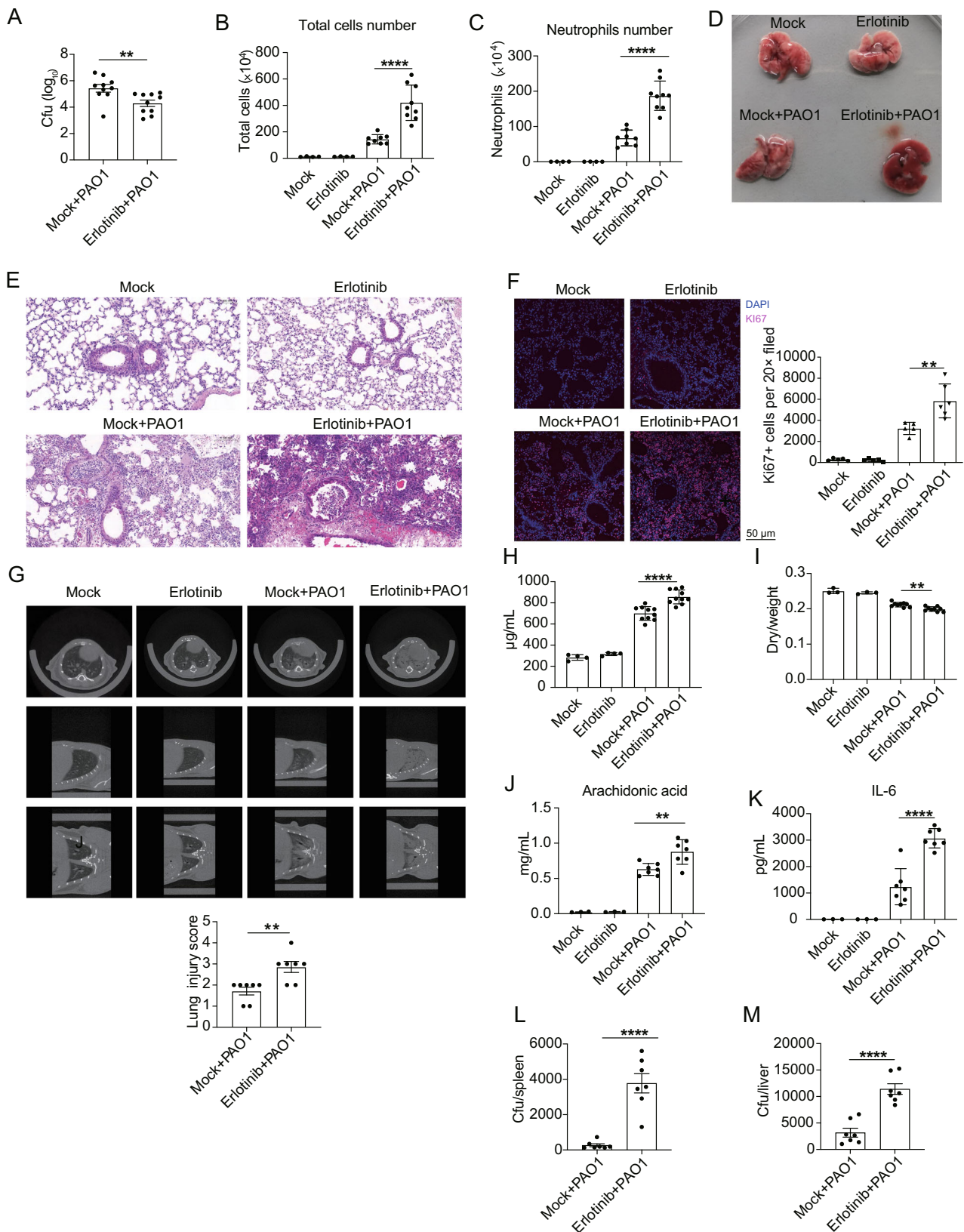
3oc12-EGFR maintains epithelial barrier through influencing tight junction protein expression

To confirm that 3oc12 regulates airway epithelial barrier integrity, we utilized an established in vitro model to check the permeability of epithelial cell paracellular pathway. A layer of A549 cells was grown on a trans-well filter surface, and different sizes of FITC-dextran were loaded into the top well and their appearance across the cell layer was measured with or without 3oc12 treatment^{49,50}. The results showed that 3oc12 was able to inhibit the movement of 4KD and 10KD FITC-dextran across the filter yet had no effect on 40KD (Fig. 7A). Transepithelial electrical resistance (TEER) is the measurement of electrical resistance across a cellular monolayer, an unbiased indicator of permeability of the monolayer cells^{51,52}. After 2- or 3-hour treatment, 3oc12 significantly increased the $\Omega \cdot \text{cm}^2$ of A549 cells at both time points (Fig. 7B).

Tight junction protein expression is the main regulator of paracellular pathway permeability^{53–55}. On mRNA level, Claudin 1, 2, 7, 8, 10, Tight Junction Proteins 2 (*TJP2*) and Junctional Adhesion Molecule 1 (*JAM-1*) were all upregulated by 3oc12 treatment (Fig. 7C). We chose Claudin-1 and Claudin-2 as representative to check the protein level expression by flow cytometry, and the results were in line with the QPCR results (Supplementary Fig. 9A). In the in vivo study, H&E and Micro-CT results demonstrated that the $\Delta lasI$ strain induced more immune cells infiltration and lung epithelial barrier disruption than did $\Delta lasR+lasI$ strain (Fig. 7D, E). The cells number, protein concentration and inflammatory cytokine levels in BALF were also lower in $\Delta lasR+lasI$ group (Supplementary Fig. 9B–I). Therefore, 3oc12 protects the host against damage brought in by *P. aeruginosa* infection mainly via maintaining epithelial barrier functions.

3oc12 maintains lung epithelial barrier through EGFR-STAT3 signaling pathway

To further confirm the presence of a 3oc12-EGFR signaling pathway, epithelial cells were pretreated with Erlotinib and their expression of tight junction protein mRNAs were analyzed. Indeed, the increased expression of Claudin 1, 2, 7, 8, 10 as well as *TJP-2* and *JAM-1* in response to 3oc12 treatment was almost completely blocked with Erlotinib treatment, confirming the effect of 3oc12 was via EGFR (Supplementary Fig. 10A). Accordingly, the reduced filtration rates across single layer lung epithelium for 4KD and 10 KD FITC-Dextran in response to 3oc12 treatment were no longer seen in the presence of Erlotinib (Fig. 8A). This was further confirmed by the TEER reading (Fig. 8B). STAT3 has been the most studied downstream target in EGFR signaling, both in



the conventional sense of a transmembrane receptor/an intracellular binding pair, also as a transcriptional factor complex in the nucleus^{56–58}. The treatment of 3oc12 induced STAT3 (Y705) phosphorylation in sync with EGFR, and both phosphorylation events were inhibited in the presence of Erlotinib, hinting that in this study STAT3 was likely involved (Fig. 8C, D). We used CRISPR-Cas9 to knock out

stat3 in A549 cells (Supplementary Fig. 10B). In the absence of STAT3, 3oc12 could no longer affect the expression of tight junction proteins, nor could it change monolayer permeability or electric conductance (Fig. 8E–G). To establish this connection in vivo, *Sftpc-ert2cre* (Surfactant protein C promoter) mice were crossed with *stat3^{fl/fl}* mice to get *Sftpc-ert2cre-stat3^{fl/fl}* mice, and the resulting adult progenies were

Fig. 6 | 3oc12-EGFR axis protects against *P. aeruginosa* dissemination in *C57BL/6* mice. **A** The cfu of *P. aeruginosa* in the lung of Erlotinib-treated and control group infected mice (7 weeks old, male, $n = 10$ per group). **B, C** The total cells and neutrophil numbers in BALF from four groups of mice ($n = 4, 4, 8, 9$). The external appearance (**D**), H&E staining (**E**) and Ki67+ staining (**F**) of lung tissue from indicated groups of mice ($n = 5, 5, 5, 6$). **G** The Micro-CT pictures of mouse lung ($n = 7$ per group). **H** The protein levels in BALF from four groups of mice ($n = 4, 4, 10, 10$). **I** The ratio of dry/wet weight of lung tissue from four groups of mice ($n = 3, 3, 9, 9$).

J The concentration of arachidonic acid in BALF ($n = 3, 3, 7, 7$). **K** The levels of serum IL-6 concentrations ($n = 3, 3, 7, 7$). **L, M** The *P. aeruginosa* cfu in spleen (**L**) and liver (**M**) from Erlotinib treated and control group infected mice ($n = 7$ per group). **Fig. F, J** are repeat for twice, **Fig. A–C, G–I, L, M** and are presented of three independent of three times. Data are presented as the mean \pm s.e.m. $^{**}P < 0.01$, $^{***}P < 0.001$, $^{****}P < 0.0001$. Two-tailed unpaired Student's *t*-tests were used to analyze data. Source data are provided as a Source Data file.

treated with tamoxifen to remove *stat3* in Alveolar Type II cells (AT2 cells) (Supplementary Fig. 10C). In this experiment, we used *Sftpc-ert2cre* mice treated with tamoxifen as control. The mice were then infected with *P. aeruginosa*. The Micro-CT results showed that the mice with *stat3* knockout in AT2 cells had no baseline abnormality in the lung, and *P. aeruginosa* infection could be established as well. Yet, in the absence of STAT3, PAOI infection was more severe with massive purulent lesions reminiscent of infection with EGFR blockage (Fig. 8H). In BALF, the group of *stat3*-deficient mice had higher protein and IL-6 concentrations than the *Sftpc-ert2cre* only control, indicating a greater damage to the lung epithelia (Fig. 8I, J). We also found higher loads of *P. aeruginosa* in spleen and liver, and a higher IL-6 level in the serum (Fig. 8K–M). These results indicate that more *P. aeruginosa* transcrossed the epithelial barrier and entered the circulation and distal organs. To directly confirm that 3oc12 in a real infection mediated its EGFR downstream effect via STAT3, we used Δ *lasI* and Δ *lasR+lasI* strains to infect AT2 *stat3*-deficient mice. As expected, the severity of pathology revealed by Micro-CT and the protein level in BALF were similar between two strains of bacteria, suggesting that the protective effect of 3oc12 was nullified in the absence of STAT3 (Supplementary Fig. 10D, E).

3oc12 exerts a general protection effect in lung acute injuries

Lung permeability increase underlies most of lung inflammatory dysfunctions, such as asthma and pulmonary infections^{7,8}. Reduced lung permeability in theory has therapeutic effects. To prove this concept, we established two acute lung injury models. 0.4 N of hydrochloric acid was mixed with equal volume of DMSO, and the mixture was delivered by inhalation at 2 μ l/g body weight. The mice were treated with 3oc12. Figure 9A–G showed HCL caused significant lung infiltration and an increase in inflammatory cytokines and protein in BALF. Remarkably, 3oc12 demonstrated a strong ability to reduce all those parameters, indicating therapeutic efficacy (Fig. 9A–G). The experiment was replicated with 10 mg/ml LPS. The 3oc12's effect was again reproduced across all measurements (Fig. 9H–N). Therefore, 3oc12-mediated EGFR signaling may be of potential clinical value in treating pulmonary inflammation and injury.

In summary, we found that 3oc12 on lung epithelial cells causes a loss of membrane order and disappearance of lipid rafts, which permits a ligand-free EGFR self-dimerization and ensuing phosphorylation. This leads to nuclear translocation of STAT3, which mediates tight junction protein expression and reduced lung epithelial permeability. This effect localizes *P. aeruginosa* infection and works against the uncontrolled dissemination in the host, which may contribute to the establishment of long-term infection (Fig. 9O).

Discussion

Lung functions depend on the integrity of the lung epithelial barrier, especially the alveolar epithelium⁵⁹. Neighboring lung epithelial cells are knitted by tight junction proteins, acting as gatekeepers to seal the paracellular space and to prevent the entry of foreign antigens that could contribute to inflammation and tissue damage^{53–55,60–62}. Loss of tight junctions in the airways results in an uncontrolled leakage of high molecular weight proteins and water, which results in severe lung inflammation and the formation of alveolar edema^{63–65}.

EGFR activation is important for the host in defense against bacterial infection^{66–68}. EGFR on the lung epithelial cells surface participates in the regulation of epithelial barrier homeostasis through controlling a series of tight junction proteins expression^{69–71}. At present, many ligands have been confirmed to activate EGFR, such as Epidermal Growth Factor (EGF), Transforming Growth Factor α (TGF α), bidirectional regulator (AR), epidermal regulator (EREG), β -cytokines and heparin-bound epidermal growth factor (HB-EGF)⁷². The large number of potential ligands suggests that EGFR may be a central coordinator of many networks of signaling in the maintenance of epithelial health. Remarkably, EGFR is probably the most documented surface receptor to be regulated by membrane biophysics^{28,31,73}, and its behavior in relationship with membrane-ordered state is used as a model to the lipid raft research.

Lipid raft is a concept first proposed by Simons et al. to describe the spontaneous presence of glycolipid and cholesterol-rich domain on the outer leaflet of the plasma membrane that regulates cell surface proteins⁷⁴. EGFR spontaneous activation upon cholesterol depletion was reported by many groups. Linda Pike et al. in 2002 reported that removal of cholesterol increased of EGFR phosphorylation, and this effect was mediated by its intrinsic kinase activities without any ligand⁷⁵. Various experimental designs have since confirmed this observation^{29–31,76–78}. We reported that on the neutrophil surface, 3oc12 caused the dissolution of lipid rafts, which led to the spontaneous trimerization of TNFR1 and cell death²⁵. This effect is less prominent in other non-immune cell types. In epithelial cells, EGFR signaling is expected to be more prevalent. Cell type-specific receptor signaling has been reported in other systems. The cause is extremely complex, and appears to have been built into the signaling network since the cellular function diversification⁷⁹. This work is our attempt to ask whether relaxation of lipid-ordered state (lipid raft removal) also permits spontaneous activation of EGFR via self-dimerization.

Our results indicated that indeed this mechanism is operational in lung epithelial cells. Our MD analysis indicated that this is mainly due to a preferred pairing of GXXXG motifs in L_d phase. Thermodynamically, while enthalpy drives EGFR dimerization regardless of L_o vs L_d phases, the formation of the dimer in L_o leads to a decrease in entropy, supporting the increase of EGFR dimerization upon 3oc12-mediated lipid raft dissolution. After this ligand-free activation, the RTK cross-phosphorylation of EGFR recruits STAT3 which mediates the higher expression of tight junction proteins. This mechanism appears to better shield the *P. aeruginosa* infection site from the rest of lung tissues, and deficiency at either *LasI*, EGFR or STAT3 leads to massive barrier breach and dissemination of the infection and a significantly higher death rate.

Pathogens and the host can hijack each other's signal pathways, collectively known as the "inter kingdom" signaling. Quorum sensing autoinducers, such as 3oc12 are known participants of this exchange^{32,80,81}. If our work is further validated, it seems to suggest the possibility that this small lipid-like structure can manage to use its ability to disrupt lipid rafts to drive two major signaling events in two groups of cells for its own survival: the aggregation of TNFR1 on neutrophils to induce the latter's apoptosis, and the dimerization of EGFR to build a barrier via regulating lung epithelial cell tight junctions. Certainly, this notion remains a proposal that requires stringent scrutiny. As 3oc12's lipid raft dissolution is a generic event that happens on mammalian cells^{25,27}, its involvement in other receptors on other cell types is an intriguing topic to be explored in future investigation.

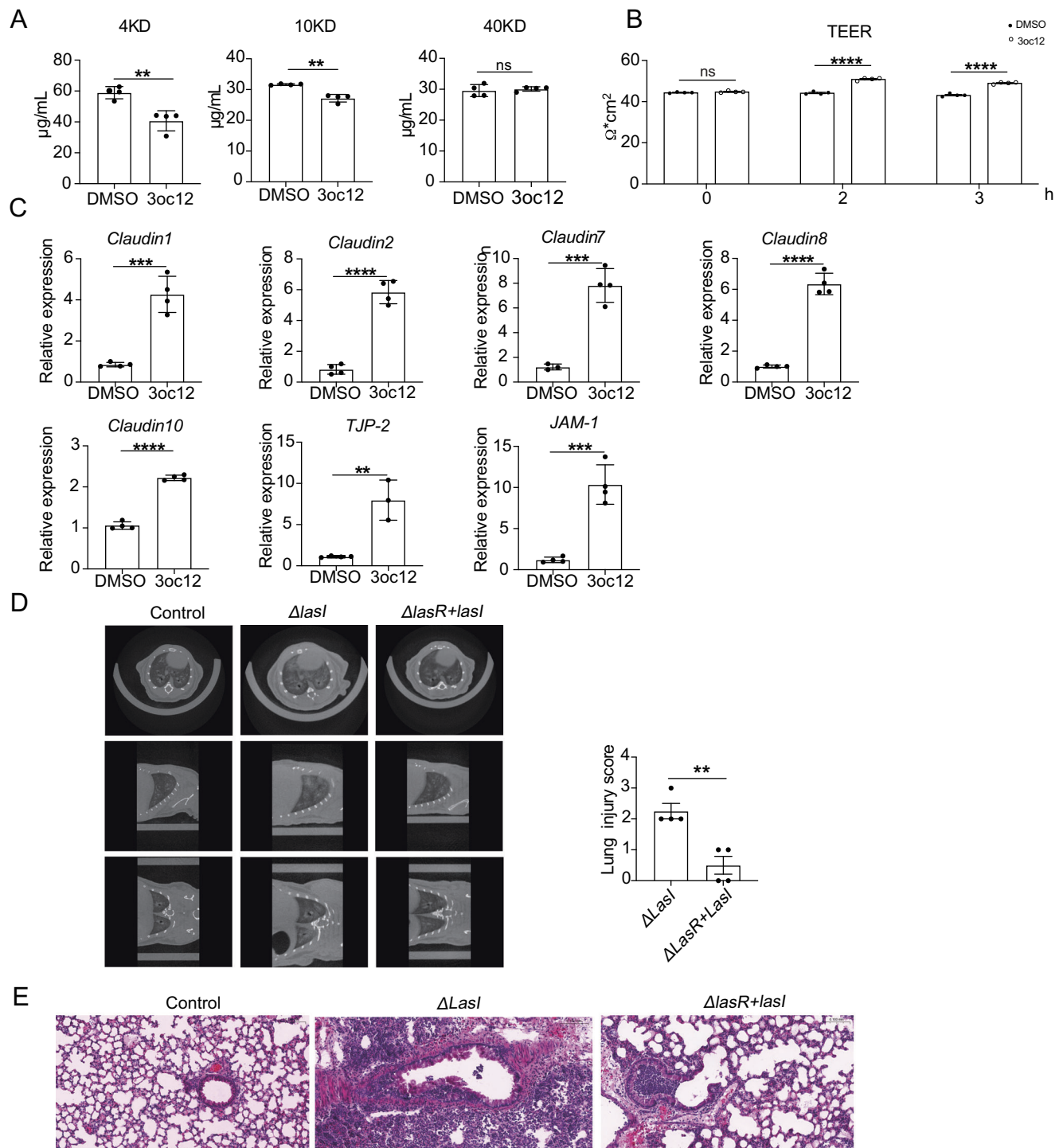


Fig. 7 | 3oc12-EGFR maintains epithelial barrier through influencing tight junction protein expression. **A** 3oc12 inhibits 4KD and 10 KD FITC-Dextran passing through the epithelial cell paracellular pathway ($n = 4$ per group). **B** 3oc12 increases the transepithelial electrical resistance of A549 monolayer cells ($n = 4$ per group). **C** 3oc12 induced multiple tight junction protein upregulation on mRNA level ($n = 3$ or 4 per group). **D** The Micro-CT of lung images in $\Delta lasI$ and $\Delta lasR+lasI$

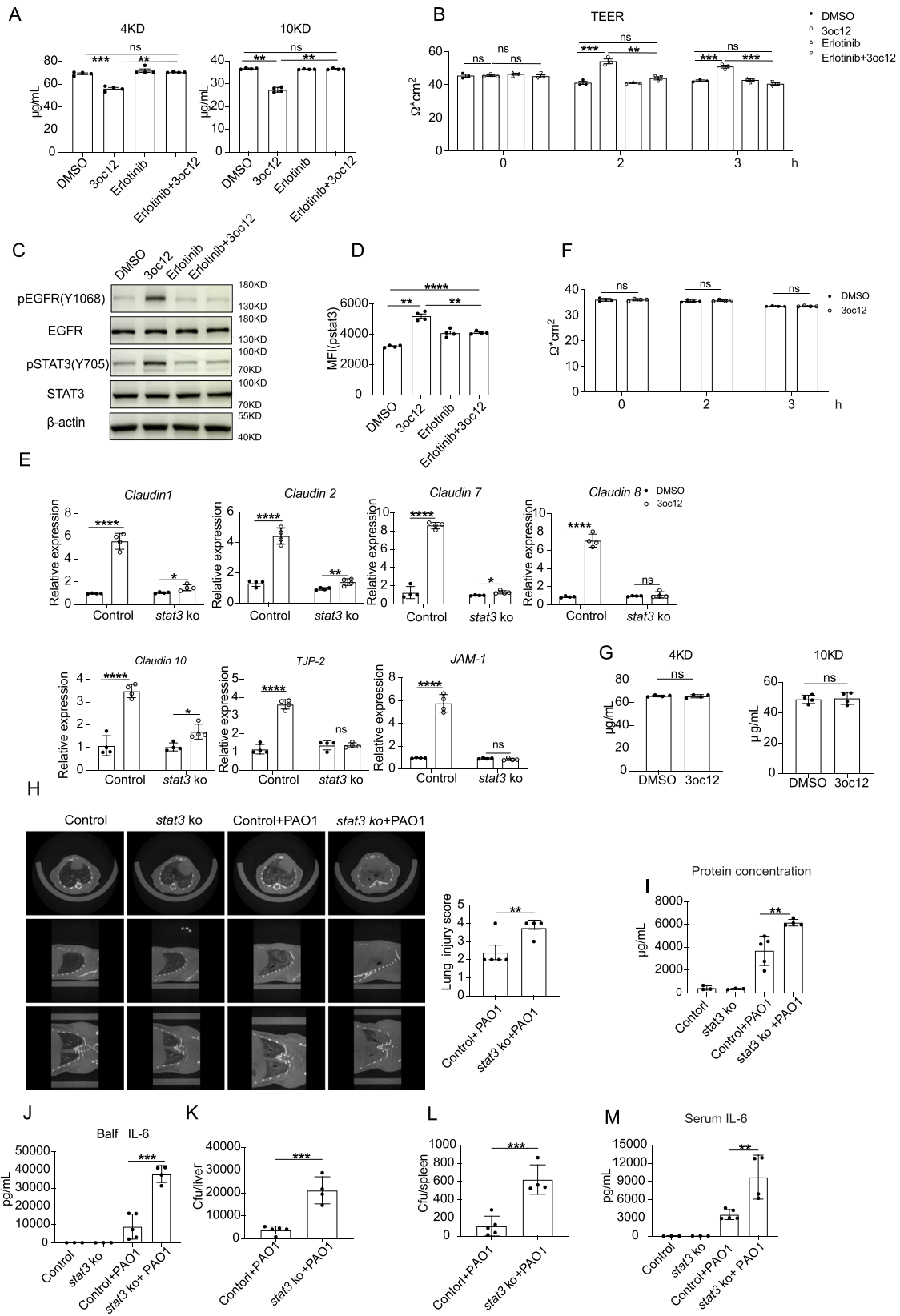
strain infected mice ($n = 4$ per group). **E** The H&E staining of lung tissue from $\Delta lasI$ or $\Delta lasR+lasI$ strains infected mice. Data are representative of three independent experiments and are presented as the mean \pm s.e.m, ** $P < 0.01$, *** $P < 0.001$, **** $P < 0.0001$. Two-tailed unpaired Student's t-tests were used to analyze data. Source data are provided as a Source Data file.

Methods

Cell culture

In vitro experiments, A549 cells, HEK293 cells, HELA cells, and MCF-7 cells were obtained from the American Type Culture Collection (ATCC). A549 cell lines were meticulously cultured in RPMI 1640 Medium, supplemented with 10% fetal bovine serum (FBS) and 1%

penicillin-streptomycin to provide optimal growth conditions. During the experimental procedures, the growth medium was replaced with serum-free RPMI 1640 during the experiment processes. HEK293 cell, HELA cell, and MCF-7 cell were cultured in DMEM medium, supplemented with 10% fetal bovine serum (FBS) and 1% penicillin-streptomycin.



Mice

In our study, mice of the C57BL/6J genetic background were utilized. Wild-type (WT) mice were purchased from Charles River. *Sftpc-ert2-cre* mice were purchased from Jackson lab, and *stat3^{fl/fl}* mice are a gift from Xiaoyu Hu laboratory (Tsinghua university). The breeding and housing

of these experimental animals were meticulously conducted within the specific pathogen-free (SPF) barrier facilities at the Tsinghua University Experimental Animal Center. The mouse model of *P. aeruginosa* infection, along with the subsequent experimental procedures, was carried out in a Biosafety Level 2 (P2 level) containment facility.

Fig. 8 | 3oc12 maintains lung epithelial barrier through EGFR-STAT3 signaling pathway. **A, B** Erlotinib can inhibit 3oc12 induced A549 cell paracellular pathway permeability ($n = 4$ per group) and Trans-epithelial resistance change ($n = 3$ per group). **C, D** Western blot and FACS to confirm 3oc12 induced STAT3 phosphorylation was through EGFR ($n = 4$ per group). **E** 3oc12 was unable to induce multiple tight junction protein upregulation in *stat3*-deficient A549 cells ($n = 4$ per group). **F, G** 3oc12 was unable to induce paracellular pathway permeability and Trans-epithelial resistance changes in *stat3*-deficient A549 cells ($n = 4$ per group). **H** The

micro-CT result of *stat3* specific knock-out in lung epithelial cells mice (12 weeks old, male mice) treated with PAOI. **I, J** The protein and IL-6 concentration in BALF from four group of mice. **K–M** The load of PA in spleen and liver, as well as serum IL-6, from control and *stat3*-specific knock-out mice. **H–M** ($n = 3, 3, 5, 4$). Data are representative of three independent experiments and are presented as the mean \pm s.e.m. $**P < 0.01$, $***P < 0.001$, $****P < 0.0001$, ns: not significant. One-way ANOVA was used for Fig. **A, B, D** analysis. Two-tailed unpaired Student's *t*-tests were used to analyze Fig. **E–G, I, H, J–M**. Source data are provided as a Source Data file.

Bacterial strains

P. aeruginosa WT PAOI, 3oc12 synthetase-deficient $\Delta lasI$, and the 3oc12 overexpressing $\Delta lasR + lasI$ were prepared and used according to our lab's previous work²⁵. The bacterial strains were cultured in LB medium or SCFM medium⁸². SCFM is particularly used to mimic the nutrient-rich environment of the cystic fibrosis lung, providing a more clinically relevant context for studying *P. aeruginosa*.

Reagents

The EGFR kinase domain inhibitors Erlotinib (S1023), PD153035(S1079), AG1478(S2728), were purchased from Selleck. EGFR (ABP0084), claudin-1(ABP0072), claudin-2 (ABP56953) were purchased from Abbkina. Phospho-EGFR Tyr1068 (3777), STAT3 (12640), phospho-stat3705(9145), β -actin (4970), were purchased from CST. Ly-6G APC (127614), ki67-PE (151210), and CD24-PE (119310) were purchased from BioLegend. EpCAM-APC (17-5791-82), CD31-PE (12-0311-81), podoplanin-PE (12-5381-80), CD45-PE (12-0451-81), Scal-PE (12-5981-81), Foxp3/Transcription Factor Staining Buffer Set (00-5523-00) were purchased from Ebioscience. DAPI (C1002) and Protein assays were performed using the BCA Protein quantitation Kit (Beyotime Biotechnology, P0012). Hieff[®] qPCR SYBR Green Master Mix(11201ES03) was purchased from Yeasen.

P. aeruginosa lung infection

In our study, six-week-old wild-type (WT) male mice were acclimatized to the Biosafety Level 2 (P2 level) animal housing facilities for one week prior to the commencement of infection experiments. This acclimatization period was critical to ensure the mice adapted to their new environment, minimizing stress-related variables that could potentially influence experimental outcomes. Each mouse was intraperitoneally injected with the anesthetic avertin (tribromoethanol) 300 μ l. Once the mice were fully anesthetized, a precisely measured inoculum of 50 μ l containing 2×10^7 colony-forming units (CFU) of *P. aeruginosa* was injected directly into the trachea. Twenty-four hours post-infection, micro-computed tomography (Micro-CT) scanning was employed to assess lung injury. This advanced imaging technique allowed for a detailed and non-invasive evaluation of the extent of lung damage caused by the bacterial infection, providing critical insights into the pathophysiology of the disease model. This careful orchestration of the experimental setup was vital for the generation of reliable and reproducible data.

Micro-CT

For imaging, mice were anesthetized with avertin and positioned on the Micro-CT scanner platform. Scanning parameters were set as follows: voltage at 90 kV, current at 88 μ A, and a resolution of 72 μ M/pixel. The scoring system of the disease was described in a previous paper⁸³(Quantum GX).

Western blotting

Cells were lysed by RIPA buffer containing protease and phosphatase inhibitors. Lysates were left on ice for 30 min then an ultrasonic wave was used to lyse cells. The concentration of protein was determined using a BCA protein quantitation kit. Sample lysates were separated by SDS-PAGE and blotted using primary antibodies overnight at 4 $^{\circ}$ C. Membranes were then incubated with horseradish peroxidase (HRP)-

conjugated secondary antibodies for 1 h at room temperature (ChemiDoc MP).

Measurement of transepithelial electrical resistance

Lung epithelial cells were seeded into 24-well Trans-well inserts (Costar Corning, 0.4 μ m). The cells were seeded at a density of 2×10^5 cells/well, the cell culture medium was changed every two days for 4 days. At the same time, set two wells without cells as blank (the cell culture inserts without cells). Two hours before the experiment, the culture medium was replaced with fresh pre-warmed medium. During the experiment, the prewarmed medium without supplements was added to the inner chamber (200 μ l) and outer chamber (400 μ l). The transepithelial electrical resistance of the cell layer was measured using Millicell-ERS equipment.

Permeability of cell monolayer

The permeability of the cell monolayer was assessed by determining FITC-dextran fluxes across this layer. Similar to TEER measurement, cells were cultured in trans-well inserts for 4 days, with medium change every two days. Cells were washed the in/outer chamber twice with pre-warmed Hank's buffer. The inserts were moved to a fresh 24-well plate containing 800 μ l of pre-warmed Hank's buffer in the outer chamber. 200 μ l of 1 mg/ml FITC-dextran solution was added to top compartment of the insert. Samples were removed from the basal compartments after 2 h. The fluorescence was measured using Envision at excitation and emission wavelengths of 492 nm and 520 nm, respectively (Envision-l).

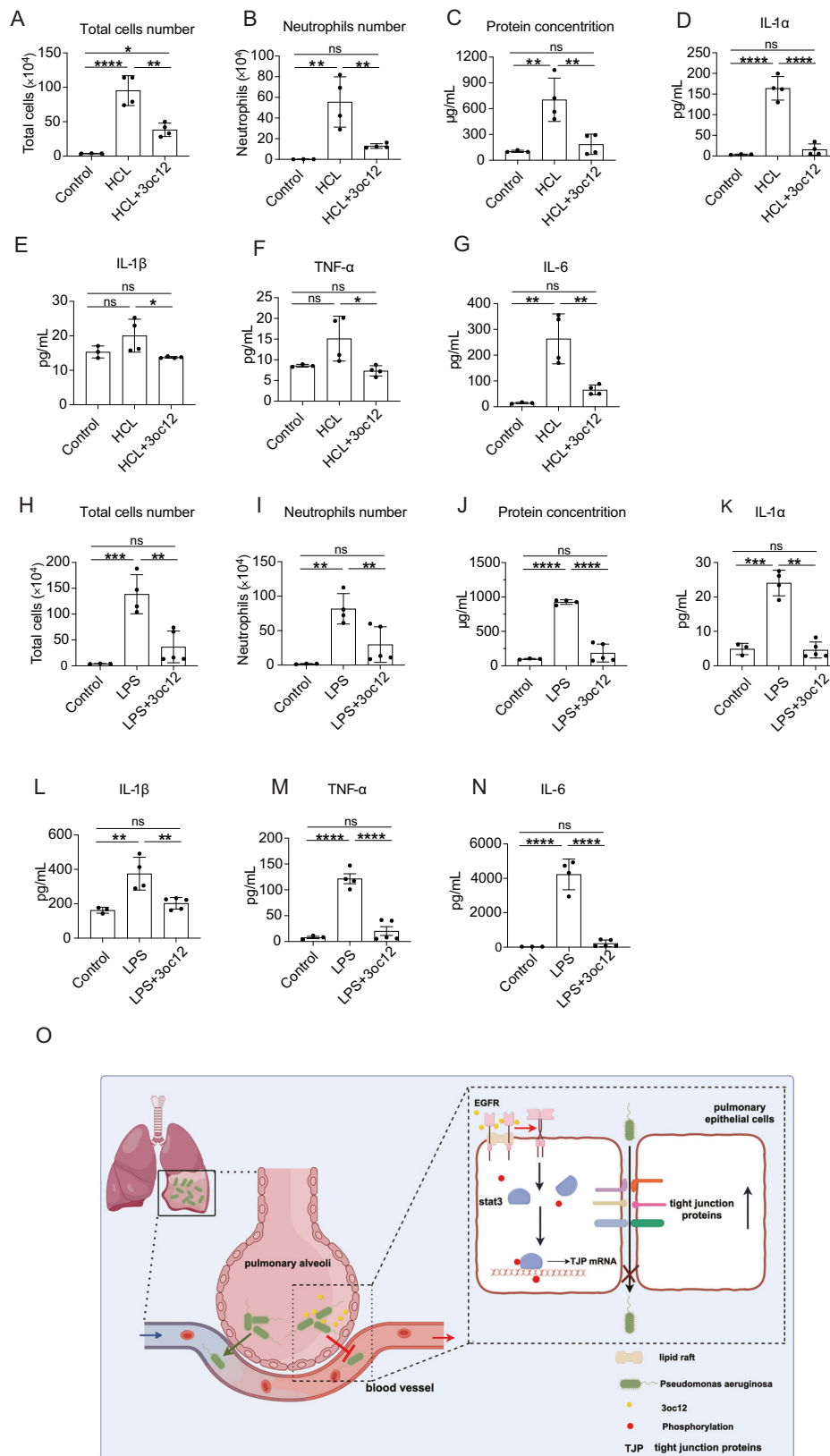
Single-molecule fluorescence tracking and diffusion subsequent analysis

To track endogenous EGFR on the cell membrane, genome editing of HEK293 cells was performed using the CRISPR/Cas9 approach to incorporate Halo tag to the C-terminus of EGFR, as described previously⁸⁴. Genome-edited HEK293 monolayers (75% confluent) previously serum-starved for 4 h were treated with 10 μ M 3oc12 or left untreated for 5 min and incubated with 2 nM of the JFX646-HaloTag ligand solution at 37 $^{\circ}$ C for 2 min. The cells were then washed twice with PBS at 37 $^{\circ}$ C, placed in phenol red-free DMEM medium, and loaded for live cell imaging. For single-molecule imaging, we employed a custom-built objective-type Total Internal Reflection Fluorescence Microscope (TIRFM). For single-molecule tracking, time-lapse series of single EGFR-Halo molecule images were acquired to 300 images per sequence at a frame rate of 12.5 Hz.

Single-particle detection and tracking were performed using the Trackmate plugin in ImageJ(v1.54 f)⁸⁵. The parameters with non-default values used a diameter of 7 pixels; a threshold of 30; a max distance of 15 pixels; a gap-closing max distance of 15 pixels; and a gap-closing max frame distance of 2 pixels. For the calculation of diffusion coefficient, we plotted the 2D mean square displacement (MSD) for each time interval Δt_n . MSD was calculated according to the following formula (1):

$$\text{MSD}(n\delta t) = \frac{1}{N-n} \sum_{i=1}^{N-n} \left\{ [x(i\delta t + n\delta t) - x(i\delta t)]^2 + [y(i\delta t + n\delta t) - y(i\delta t)]^2 \right\}$$

in which, Δt_n ($\Delta t_n = n\delta t$, with $\delta t = 100$ ms) is the elapsed time a single EGFR-Halo molecule from position $x(i\delta t)$, $y(i\delta t)$ moves to $x(i\delta t + n\delta t)$,



$y(i\delta t + n\delta t)$. n and i are integers. n represents the time increment and takes on values 1, 2, 3... $N-1$. N is the total number of image frames before the molecule disappears. According to $MSD_{t \rightarrow 0} = 4D\Delta t_n$, the slope of the first five points was used to determine the diffusion coefficient (D) via least squares fitting the $MSD-\Delta t_n$ plot. The tracks longer than 20 frames were used for MSD analysis. The upper limit of

the lag time n used in the calculation of MSD is 5. The classification of the movements of individual tracks was conducted using DC-MSS⁸⁶.

Single-Molecule Fluorescence Bleaching Trajectory Extraction
For individual EGFR fluorescence imaging on the cell membrane, MCF7 cells were plated in 35 mm glass-bottomed dishes that had been coated

Fig. 9 | 3oc12 exerts a general protection effect in lung injuries. A–G 3oc12 can rescue the HCL-induced acute lung injury. The total cell number, neutrophil number, protein levels as well as IL-1 α , IL-1 β , TNF- α , IL-6 levels in BALF, respectively, are shown ($n = 3,4,4$). H–N similar to A–G, 3oc12 effects in the LPS-induced acute lung injury ($n = 3,4,5$). Data are representative of three independent experiments and are presented as the mean \pm s.e.m. * $P < 0.05$, ** $P < 0.01$, *** $P < 0.001$, **** $P < 0.0001$. One-way ANOVA was used to analyze the data. O The model of 3oc12 involved in maintaining the host epithelial barrier during *P. aeruginosa* infection. 3oc12 induces spontaneous activation of the EGFR by disrupting the lipid raft structures on the host cell

membrane. This disruption leads to the phosphorylation of EGFR and the downstream STAT3, which subsequently results in the upregulation of tight junction proteins' expression. The increased expression of these proteins effectively reduces the permeability of the paracellular pathway. Consequently, this reduction in permeability acts as a barrier to inhibit the diffusion of *P. aeruginosa* through the epithelia. This mechanism may suggest a crucial cellular defense strategy to limit bacterial invasion, emphasizing the role of tight junctions in maintaining the epithelial integrity. Fig. 9O was created using the Figdraw website and permission for its use has been obtained. Source data are provided as a Source Data file.

by poly-D-lysine (PDL). Prior to imaging, the cells were serum-starved and transfected with EGFR-mEGFP plasmids using Lipofectamine 3000 (Thermo Fisher Scientific), following the manufacturer's instructions, for a duration of 6 h. Following transfection, the cells were washed twice with PBS, fixed by 4% (w/v) paraformaldehyde for 25 min at room temperature, and then imaged in phenol-free DMEM. For single-molecule imaging, we employed a custom-built objective-type TIRFM, based on the Olympus IX71 inverted microscope platform. The fluorescence from mEGFP was excited by a solid laser (a laser line at 488 nm), and the emitted light was collected by the oil immersion objective (100 \times , 1.45NA, Olympus), and then separated by the dual-view assembly (Optical Insights). After being filtered by band-pass filter, it was projected onto an electron multiplexing charge coupled camera (EMCCD, Andor technology du-897d-bv). The gain of EMCCD was set to 300. The power of excitation light measured after passing through the objective lens was modulated to 1 mW in epifluorescence mode for cell imaging. Micromanager software and z-axis negative feedback equipment (MFC-2000) were used to control image acquisition. Movies consisting of 300 frames were acquired at a frame rate of 10 Hz for each cell. The method for extracting single-molecule fluorescence photobleaching steps of single EGFR molecules was adapted from the processing techniques described in our previously published paper^{87,88}. Briefly, the background fluorescence was subtracted using the rolling ball method in ImageJ software. Subsequently, the first five frames of each movie were averaged to create a reference image. This averaged image was then thresholded and filtered for intensity analysis. Finally, time courses of integrated fluorescence intensity were extracted from the processed movies, allowing for the analysis of single-molecule photobleaching events of EGFR on the cell membrane.

Structured Illumination Microscopy

To investigate the morphology of the actin cytoskeleton upon 3oc12 treatment, cells were prepared as described above for single-molecule imaging and stimulated with either 375/500 nM latrunculin B (Abcam, ab144291) for 30 min (positive control), 10 μ M 3oc12 for 5 min, or left untreated. The cells were then fixed and permeabilized for 10 min at room temperature with 3.7% paraformaldehyde and 0.1% Triton X-100. A single 5-minute wash with PBS was followed by a post-fix with 3.7% paraformaldehyde as above. The actin cytoskeleton was then stained with phalloidin-Atto 647 N (Sigma, 65906, 1:200) in a 5% BSA/PBS solution. Staining was performed in the dark at room temperature for 1 hour, followed by three 5-minute PBS washes. The fluorescent actin cytoskeleton images were obtained using a Multi-SIM system (NanoInsight-Tech) equipped with a 100 \times /1.49NA objective and recorded using an Photometrics (Kinetix, 1536 \times 1536 pixels) for a maximum field of view of 94 \times 94 μ m. The illumination mode was TIRF for cortical actin filaments imaging and Low NA for stress fibers imaging. A camera exposure time of 30 ms was used. The cellular actin cytoskeleton was quantified by calculating the average fluorescence intensity of actin filaments per unit cell area.

Colocalization analysis of EGFR with lipid raft

Genome-edited HEK293 cells expressing EGFR-Halo were grown overnight in 4-well confocal dishes (Cellvis). Following a 6-hour

starvation period, the cells were treated according to experimental conditions and subsequently fixed with 3% paraformaldehyde and 0.1% glutaraldehyde for 10 min at room temperature. The fixed cells were then blocked with 5% bovine serum albumin (BSA) in PBS for 1 hour at room temperature. For staining, the cells were sequentially incubated with two solutions: Alexa555-conjugated Cholera toxin-B (Invitrogen, 1:200 dilution) in 5% BSA/PBS for 30 min, followed by 2 nM JFX646-HaloTag ligand in PBS for 2 min at room temperature. After each staining step, the cells were rinsed three times with PBS to ensure specificity. A post-fixation step using the same fixation protocol was performed, followed by a single PBS wash. For dual-color TIRF imaging, the stained samples were excited sequentially using a 647 nm laser to visualize EGFR and a 561 nm laser to capture lipid raft imaging. The colocalization analysis was performed in an object-based correlation manner by program package in MATLAB (MathWorks).

Molecular dynamics simulation

The simulation systems considered in this study consisted of proteins, lipids, and solvent molecules. Two membrane systems, referred to as the L_o system and the L_d system, were constructed to simulate the lipid raft and non-lipid raft regions, respectively (Fig. S1). The upper leaflet of the L_o phase membrane consisted of [3-hydroxy-2-(tetra-cosanoylamino) octadecyl] 2- (trimethylazaniumyl) ethyl phosphate (DSM) and cholesterol (CHOL) in a ratio of 2:1, while the lower leaflet consisted of pure 1,2-distearoyl-sn-glycero-3-phosphocholine (DSPC) lipids^{89,90}. The L_d phase membrane was composed of pure 1,2-dioleoyl-sn-glycero-3-phosphocholine (DOPC) lipids. These two combinations of lipid components have been widely used in previous simulations of plasma membranes under distinct phase states⁹¹. To examine whether 3oc12 molecules can penetrate through the membrane and interact with PI(4,5)P2 in the inner leaflet to influence EGFR dimerization, we prepared a simulation system, where nine 3oc12 molecules were positioned above the membrane with six PI(4,5)P2 molecules randomly distributed in the inner leaflet. The transmembrane domain (residues 610-653) of EGFR was extracted from the protein data bank (PDB) entry 5LV6⁴⁴. Structures of the juxtamembrane domain (residues 610-677) and extracellular domain (residues 1-653) were obtained from the PDB entry 2M20⁴⁷ and 1IVO⁹², respectively. The lipid bilayer membranes involved with different proteins were built by the online-tool CHARMM-GUI⁹³. Based on the size of the protein models, the dimensions of the simulation systems were set to 7.5 \times 7.5 \times 10.7 nm³ (transmembrane domain), 12.5 \times 12.5 \times 13.5 nm³ (transmembrane and juxtamembrane domains), and 14 \times 14 \times 21 nm³ (transmembrane and extracellular domains). The CHARMM36 force field was used for both proteins and lipids, and water molecules were represented by TIP3P model⁹⁴. After solvation of the simulation system by water, Na⁺ and Cl⁻ ions were added to neutralize the system charge and represent the normal ionic strength of 0.15 M. The protonation states of residues were determined according to pH = 7.

Each simulation system contained either two monomers of EGFR (initial distance of 2 nm) or one dimer to compare the interaction energy between different components. All-atom MD simulations were performed using the GROMACS 4.6.7 software package to observe the behavior of EGFR within various membrane environments⁹⁵. Initially, energy minimization was carried out by the steepest descent method

to remove bad initial contacts. Subsequently, the systems were pre-equilibrated using 6-step equilibrations generated by CHARMM-GUI⁹⁶. During this process, the proteins were restrained in their initial positions and then the restraints were removed. Each system was then simulated for 200 ns in the NPT ensemble at $T = 310\text{ K}$ and $p = 1\text{ bar}$. Temperature coupling was achieved using the Nose-Hoover thermostat, and pressure coupling was maintained by the Parrinello-Rahman barostat. Nonbonded interactions were cutoff at 1.2 nm, and long-range electrostatic interactions were treated with the particle-mesh Ewald summation method. A time step of 2 fs was performed, with the neighbor list updated every 20 steps. Periodic boundary conditions were applied in all three directions.

To investigate the preferred membrane phase for EGFR dimerization, we established a model plasma membrane containing L_o and L_d phases, with five EGFR dimers pre-positioned at the phase boundary. A coarse-grained model was employed to address the size and time scale limitations of the system. The system dimensions are $25 \times 55 \times 10.5\text{ nm}^3$, and the lipid composition matches that described previously. The Martini 2.2 coarse-grained (CG) force field was used for both proteins and lipids⁹⁷. Using identical parameters to the prior setup, proteins and lipid head groups were restrained during a 100 ns pre-equilibration simulation. Subsequently, these restraints were removed, and a 4 μs production simulation was conducted in the NPT ensemble. Temperature was maintained using the V-rescale thermostat, and pressure was regulated using the Parrinello-Rahman barostat. The cutoff distance for short-range interactions was set to 1.1 nm, with periodic boundary conditions applied in all three directions. The simulation time step was 20 fs, and the neighbor list was updated every 20 steps. Trajectory analysis and visualization were conducted using VMD 1.9.3⁹⁸.

Isolation of murine AT2

For the isolation of alveolar type 2 (AT2) cells from lung tissues, initially, lung tissues were carefully dissected into small pieces using sterilized scissors. These tissue fragments were then subjected to enzymatic digestion using a solution of collagenase III at a concentration of 1 mg/ml and DNase I at 20 $\mu\text{g/ml}$, prepared in RPMI-1640 medium supplemented with 1% fetal bovine serum (FBS). This digestion was carried out at 37 °C for 40 min, with periodic mechanical agitation (shocks) to facilitate the breakdown of tissue into single cells. Following digestion, the resultant cell suspension was filtered through a 70 μm cell strainer to remove any undigested tissue fragments and to ensure a uniform single-cell suspension. Then the digested medium was passed through 70 μm filter and the single-cell suspensions were stained with EpCAM-APC, CD31-PE, CD45-PE, podoplanin-PE, Scal-PE, CD24-PE and DAPI. To isolate the AT2 cells, we employed flow cytometry gating strategies, specifically selecting for cells that were APC positive and PE negative cell population to obtain AT2 cells (Aria III-2020 Configuration).

Construction of *stat3* knockout cell line

To achieve the knockout of the *stat3* gene in human lung epithelial A549 cells, we employed CRISPR-Cas9 method. The gRNA sequences (from 5'–3'): GAAACTGCCGACGCTCCATT, AATGGAGCTGCGG-CAGTTTC. Phosphorylated gRNA oligos were linked to LentiCRISPR lentiviral plasmid with GFP-tag. LentiCRISPR, psPAX2, pMD2.G plasmids were transfected into A549 cells. GFP-positive cells were sorted three times and seeded to 96-well plate at one cell/well to get monoclonal cell lines. To confirm the successful knockout of *stat3*, Western blot analysis was performed.

Lung epithelia specific STAT3 knock-out

We used *Sftpc-cre-ert2* mice cross with *stat3^{fl/fl}* mice to obtain *Sftpc-cre-ert2 stat3^{fl/fl}* mice. Tamoxifen was dissolved in corn oil in a concentration

of 20 mg/ml and delivered via intraperitoneal injection at a dose of 75 mg/kg body weight for five days. Fourteen days after the completion of the tamoxifen treatment, alveolar type 2 (AT2) cells were isolated from the mice for the purpose of assessing the efficiency of the *stat3* gene knockout.

HCL or LPS -induced acute lung injury

Mice were anaesthetized and then induced for acute lung injury with HCL or LPS by intranasal instillation. Injury was induced by instilling 2 $\mu\text{l/g}$ of osmotically balanced 0.4 N HCL or 10 mg/mL LPS. Twenty-four hours following the instillation, mice were sacrificed to collect BALF, serum and lung tissue for analysis.

Intracellular staining

For measurement claudin1 and claudin2 expression, 3oc12 or bacteria culture media treated epithelial cells were washed by cold PBS. Subsequently, these cells were fixed and permeabilized with the Foxp3/Transcription Factor Staining Buffer Set according to the manufacturer's instructions. After fixation and permeabilization, these cells were stained with specific antibodies: anti-claudin1 or anti-claudin2 for 30 min in 4 °C (Fortessa 4 laser).

RNA extraction and RT-PCR

RNA was extracted by trizol from whole cell lysates and was reversely transcribed to cDNA according to manufacturer's instructions. RT-PCR was performed with Hieff® qPCR SYBR Green Master Mix in triplicates on a CFX96 real-time system (Bio-Rad). Samples were normalized to the expression of the gene encoding β -actin. Primer sequences were listed in the Table S1.

Quantification and statistical analysis

The data analysis and plotting were completed using Prism software (prism10). Two-tailed unpaired Student's *t*-test was used for comparing between 2 groups. One-way ANOVA with was used for multiple comparisons among 3 or more groups. Data were shown as the mean \pm sem, unless indicated otherwise. Kaplan-Meier log-rank was used for the survival analysis test. *P* value of <0.05 was considered significant: **P* < 0.05; ***P* < 0.01; ****P* < 0.001, *****P* < 0.0001; ns, not significant.

Ethics statement

All animal experiments conducted in this study received approval from the Institutional Animal Care and Use Committee (IACUC) of Tsinghua University Guidelines (GB/T35892-2018).

Reporting summary

Further information on research design is available in the Nature Portfolio Reporting Summary linked to this article.

Data availability

All the data are available in the article and its Supplementary files. Source data are provided with this paper.

References

- Hu, F. et al. Resistance reported from China antimicrobial surveillance network (CHINET) in 2018. *Eur. J. Clin. Microbiol. Infect. Dis.* **38**, 2275–2281 (2019).
- Jones, R. N. Microbial etiologies of hospital-acquired bacterial pneumonia and ventilator-associated bacterial pneumonia. *Clin. Infect. Dis.* **51**, S81–S87 (2010).
- Weinstein, R. obertA. S.E. Overview of Nosocomial Infections Caused by Gram-Negative Bacilli. *Clin. Infect. Dis.* **41**, 848–854 (2005).
- Qin, S. et al. *Pseudomonas aeruginosa*: pathogenesis, virulence factors, antibiotic resistance, interaction with host, technology

- advances and emerging therapeutics. *Signal Transduct. Target Ther.* **7**, 199 (2022).
5. Vidailiac, C. & Chotirmall, S. H. *Pseudomonas aeruginosa* in bronchiectasis: infection, inflammation, and therapies. *Expert Rev. Respir. Med.* **15**, 649–662 (2021).
 6. Gellatly, S. L. & Hancock, R. E. *Pseudomonas aeruginosa*: new insights into pathogenesis and host defenses. *Pathog. Dis.* **67**, 159–173 (2013).
 7. Fan, E., Brodie, D. & Slutsky, A. S. Acute respiratory distress syndrome: advances in diagnosis and treatment. *JAMA* **319**, 698–710 (2018).
 8. Lindsey, A. S. et al. Analysis of pulmonary vascular injury and repair during *Pseudomonas aeruginosa* infection-induced pneumonia and acute respiratory distress syndrome. *Pulm. Circ.* **9**, 2045894019826941 (2019).
 9. Hotchkiss, R. S., Monneret, G. & Payen, D. Immunosuppression in sepsis: a novel understanding of the disorder and a new therapeutic approach. *Lancet Infect. Dis.* **13**, 260–268 (2013).
 10. Berube, B. J., Rangel, S. M. & Hauser, A. R. *Pseudomonas aeruginosa*: breaking down barriers. *Curr. Genet* **62**, 109–113 (2016).
 11. Holmes, C. L., Anderson, M. T., Mobley, H. L. T. & Bachman, M. A. Pathogenesis of Gram-Negative Bacteremia. *Clin. Microbiol. Rev.* **34**, 1–27 (2021).
 12. Hauser, A. R. The type III secretion system of *Pseudomonas aeruginosa*: infection by injection. *Nat. Rev. Microbiol* **7**, 654–665 (2009).
 13. Magret, M. et al. Bacteremia is an independent risk factor for mortality in nosocomial pneumonia: a prospective and observational multicenter study. *Crit. Care* **15**, R62 (2011).
 14. Mukherjee, S. & Bassler, B. L. Bacterial quorum sensing in complex and dynamically changing environments. *Nat. Rev. Microbiol.* **17**, 371–382 (2019).
 15. Bryan, A. et al. Human transcriptome analysis reveals a potential role for active transport in the metabolism of *Pseudomonas aeruginosa* autoinducers. *Microbes Infect.* **12**, 1042–1050 (2010).
 16. Mayer, M. L., Sheridan, J. A., Blohmke, C. J., Turvey, S. E. & Hancock, R. E. The *Pseudomonas aeruginosa* autoinducer 3O-C12 homoserine lactone provokes hyperinflammatory responses from cystic fibrosis airway epithelial cells. *PLoS One* **6**, e16246 (2011).
 17. Karlsson, T., Turkina, M. V., Yakymenko, O., Magnusson, K. E. & Vikstrom, E. The *Pseudomonas aeruginosa* N-acylhomoserine lactone quorum sensing molecules target IQGAP1 and modulate epithelial cell migration. *PLoS Pathog.* **8**, e1002953 (2012).
 18. Smith, R. S. et al. IL-8 production in human lung fibroblasts and epithelial cells activated by the *Pseudomonas* autoinducer N-3-oxododecanoyl homoserine lactone is transcriptionally regulated by NF- κ B and activator protein-2. *J. Immunol.* **167**, 366–374 (2001).
 19. Grabiner, M. A. et al. *Pseudomonas aeruginosa* quorum-sensing molecule homoserine lactone modulates inflammatory signaling through PERK and eIF2 α . *J. Immunol.* **193**, 1459–1467 (2014).
 20. Guo, J., Yoshida, K., Ikegame, M. & Okamura, H. Quorum sensing molecule N-(3-oxododecanoyl)-L-homoserine lactone: An all-rounder in mammalian cell modification. *J. Oral. Biosci.* **62**, 16–29 (2020).
 21. Li, Y. et al. N-3-(oxododecanoyl)-L-homoserine lactone promotes the induction of regulatory T-cells by preventing human dendritic cell maturation. *Exp. Biol. Med.* **240**, 896–903 (2015).
 22. Bortolotti, D. et al. *Pseudomonas aeruginosa* Quorum Sensing Molecule N-(3-Oxododecanoyl)-L-Homoserine-Lactone Induces HLA-G Expression in Human Immune Cells. *Infect. Immun.* **83**, 3918–3925 (2015).
 23. Glucksam-Galnoy, Y. et al. The bacterial quorum-sensing signal molecule N-3-oxo-dodecanoyl-L-homoserine lactone reciprocally modulates pro- and anti-inflammatory cytokines in activated macrophages. *J. Immunol.* **191**, 337–344 (2013).
 24. Jahoor, A. et al. Peroxisome proliferator-activated receptors mediate host cell proinflammatory responses to *Pseudomonas aeruginosa* autoinducer. *J. Bacteriol.* **190**, 4408–4415 (2008).
 25. Song, D. et al. *Pseudomonas aeruginosa* quorum-sensing metabolite induces host immune cell death through cell surface lipid domain dissolution. *Nat. Microbiol* **4**, 97–111 (2019).
 26. Davis, B. M., Jensen, R., Williams, P. & O’Shea, P. The interaction of N-acylhomoserine lactone quorum sensing signaling molecules with biological membranes: implications for inter-kingdom signaling. *PLoS One* **5**, e13522 (2010).
 27. Ruan, H. et al. N-(3-Oxododecanoyl) Homoserine Lactone Is a Generalizable Plasma Membrane Lipid-Ordered Domain Modifier. *Front. Physiol.* **12**, 758458 (2021).
 28. Shi, Y., Ruan, H., Xu, Y. & Zou, C. Cholesterol, Eukaryotic Lipid Domains, and an Evolutionary Perspective of Transmembrane Signaling. *Cold Spring Harbor perspectives in biology* (2023).
 29. Lambert, S., Vind-Kezunovic, D., Karvinen, S. & Gniadecki, R. Ligand-independent activation of the EGFR by lipid raft disruption. *J. Invest. Dermatol.* **126**, 954–962 (2006).
 30. Chen, X. & Resh, M. D. Cholesterol depletion from the plasma membrane triggers ligand-independent activation of the epidermal growth factor receptor. *J. Biol. Chem.* **277**, 49631–49637 (2002).
 31. Lambert, S., Ameels, H., Gniadecki, R., Herin, M. & Poumay, Y. Internalization of EGF receptor following lipid rafts disruption in keratinocytes is delayed and dependent on p38 MAPK activation. *J. Cell Physiol.* **217**, 834–845 (2008).
 32. Turkina, M. V. & Vikstrom, E. Bacteria-Host Crosstalk: Sensing of the Quorum in the Context of *Pseudomonas aeruginosa* Infections. *J. Innate Immun.* **11**, 263–279 (2019).
 33. Montagut, E. J. & Marco, M. P. Biological and clinical significance of quorum sensing alkylquinolones: current analytical and bioanalytical methods for their quantification. *Anal. Bioanal. Chem.* **413**, 4599–4618 (2021).
 34. Bag, N., Huang, S. & Wohland, T. Plasma Membrane Organization of Epidermal Growth Factor Receptor in Resting and Ligand-Bound States. *Biophys. J.* **109**, 1925–1936 (2015).
 35. Delcanale, P. et al. Aptamers with Tunable Affinity Enable Single-Molecule Tracking and Localization of Membrane Receptors on Living Cancer Cells. *Angew. Chem. Int Ed. Engl.* **59**, 18546–18555 (2020).
 36. Suzuki, K. G. et al. Transient GPI-anchored protein homodimers are units for raft organization and function. *Nat. Chem. Biol.* **8**, 774–783 (2012).
 37. Tao, R. H. & Maruyama, I. N. All EGF(ErbB) receptors have preformed homo- and heterodimeric structures in living cells. *J. Cell Sci.* **121**, 3207–3217 (2008).
 38. Needham, S. R. et al. EGFR oligomerization organizes kinase-active dimers into competent signalling platforms. *Nat. Commun.* **7**, 13307 (2016).
 39. Hummert, J. et al. Photobleaching step analysis for robust determination of protein complex stoichiometries. *Mol. Biol. Cell* **32**, ar35 (2021).
 40. Fu, Y. et al. Axial superresolution via multiangle TIRF microscopy with sequential imaging and photobleaching. *Proc. Natl. Acad. Sci. USA* **113**, 4368–4373 (2016).
 41. Boggara, M., Athmakuri, K., Srivastava, S., Cole, R. & Kane, R. S. Characterization of the diffusion of epidermal growth factor receptor clusters by single particle tracking. *Biochim. Biophys. Acta (BBA) - Biomemb.* **1828**, 419–426 (2013).
 42. Abd Halim, K. B., Koldsø, H. & Sansom, M. S. P. Interactions of the EGFR juxtamembrane domain with PIP2-containing lipid bilayers: Insights from multiscale molecular dynamics simulations. *Biochim. Biophys. Acta (BBA) - Gen. Subj.* **1850**, 1017–1025 (2015).

43. Maeda, R., Tamagaki-Asahina, H., Sato, T., Yanagawa, M. & Sako, Y. Threonine phosphorylation regulates the molecular assembly and signaling of EGFR in cooperation with membrane lipids. *J. Cell Sci.* **135** (2022).
44. Bocharov, E. V. et al. The conformation of the epidermal growth factor receptor transmembrane domain dimer dynamically adapts to the local membrane environment. *Biochemistry* **56**, 1697–1705 (2017).
45. Hedger, G., Shorthouse, D., Koldsø, H. & Sansom, M. S. P. Free energy landscape of lipid interactions with regulatory binding sites on the transmembrane domain of the EGF receptor. *J. Phys. Chem. B* **120**, 8154–8163 (2016).
46. Herrera, F. E. & Pantano, S. Structure and dynamics of nano-sized raft-like domains on the plasma membrane. *J. Chem. Phys.* **136** (2012).
47. Endres, N. F. et al. Conformational coupling across the plasma membrane in activation of the EGF receptor. *Cell* **152**, 543–556 (2013).
48. Paris, A. J. et al. STAT3-BDNF-TrkB signalling promotes alveolar epithelial regeneration after lung injury. *Nat. Cell Biol.* **22**, 1197–1210 (2020).
49. Strengert, M. & Knaus, U. G. Analysis of epithelial barrier integrity in polarized lung epithelial cells. *Methods Mol. Biol.* **763**, 195–206 (2011).
50. Gon, Y. et al. DsRNA disrupts airway epithelial barrier integrity through down-regulation of claudin members. *Allergol. Int.* **65**, S56–S58 (2016).
51. Srinivasan, B. et al. TEER measurement techniques for in vitro barrier model systems. *J. Lab Autom.* **20**, 107–126 (2015).
52. Nazari, H. et al. Advances in TEER measurements of biological barriers in microphysiological systems. *Biosens. Bioelectron.* **234**, 115355 (2023).
53. Gunzel, D. & Yu, A. S. Claudins and the modulation of tight junction permeability. *Physiol. Rev.* **93**, 525–569 (2013).
54. Koval, M. Claudin heterogeneity and control of lung tight junctions. *Annu. Rev. Physiol.* **75**, 551–567 (2013).
55. Schlingmann, B., Molina, S. A. & Koval, M. Claudins: Gatekeepers of lung epithelial function. *Semin. Cell Dev. Biol.* **42**, 47–57 (2015).
56. Song, X., Tang, W., Peng, H., Qi, X. & Li, J. FGFR leads to sustained activation of STAT3 to mediate resistance to EGFR-TKIs treatment. *Invest N. Drugs* **39**, 1201–1212 (2021).
57. Ung, N. et al. Anti-EGFR therapeutic efficacy correlates directly with inhibition of STAT3 activity. *Cancer Biol. Ther.* **15**, 623–632 (2014).
58. Grandis, J. R. et al. Requirement of Stat3 but not Stat1 activation for epidermal growth factor receptor-mediated cell growth in vitro. *J. Clin. Invest* **102**, 1385–1392 (1998).
59. Guillot, L. et al. Alveolar epithelial cells: master regulators of lung homeostasis. *Int J. Biochem. Cell Biol.* **45**, 2568–2573 (2013).
60. Milatz, S. et al. Claudin-3 acts as a sealing component of the tight junction for ions of either charge and uncharged solutes. *Biochim. Biophys. Acta* **1798**, 2048–2057 (2010).
61. Koval, M. Tight junctions, but not too tight: fine control of lung permeability by claudins. *Am. J. Physiol. Lung Cell Mol.* **29**, L217–L218 (2009).
62. Larsen, E. H., Willumsen, N. J., Mobjerg, N. & Sorensen, J. N. The lateral intercellular space as osmotic coupling compartment in isotonic transport. *Acta Physiol.* **195**, 171–186 (2009).
63. Sweerus, K. et al. Claudin-18 deficiency is associated with airway epithelial barrier dysfunction and asthma. *J. Allergy Clin. Immunol.* **139**, 72–81.e71 (2017).
64. LaFemina, M. J. et al. Claudin-18 deficiency results in alveolar barrier dysfunction and impaired alveologenesis in mice. *Am. J. Respir. Cell Mol. Biol.* **51**, 550–558 (2014).
65. Swenson, K. E. & Swenson, E. R. Pathophysiology of Acute Respiratory Distress Syndrome and COVID-19 Lung Injury. *Crit. Care Clin.* **37**, 749–776 (2021).
66. Monticelli, L. A. et al. IL-33 promotes an innate immune pathway of intestinal tissue protection dependent on amphiregulin-EGFR interactions. *Proc. Natl. Acad. Sci. USA* **112**, 10762–10767 (2015).
67. Ho, J. et al. Candidalysin activates innate epithelial immune responses via epidermal growth factor receptor. *Nat. Commun.* **10**, 2297 (2019).
68. Seo, G. S. et al. Hirsutenone reduces deterioration of tight junction proteins through EGFR/Akt and ERK1/2 pathway both converging to HO-1 induction. *Biochem Pharm.* **90**, 115–125 (2014).
69. Tang, X. et al. Epidermal Growth Factor and Intestinal Barrier Function. *Mediators Inflamm.* **2016**, 1927348 (2016).
70. Garcia-Hernandez, V. et al. EGF regulates claudin-2 and -4 expression through Src and STAT3 in MDCK cells. *J. Cell Physiol.* **230**, 105–115 (2015).
71. Chen, S. P. et al. Effects of transdifferentiation and EGF on claudin isoform expression in alveolar epithelial cells. *J. Appl. Physiol.* (1985) **98**, 322–328 (2005).
72. Sibilio, M. et al. The epidermal growth factor receptor: from development to tumorigenesis. *Differentiation* **75**, 770–787 (2007).
73. Balbis, A. & Posner, B. I. Compartmentalization of EGFR in cellular membranes: role of membrane rafts. *J. Cell Biochem* **109**, 1103–1108 (2010).
74. Simons, K. & Ikonen, E. Functional rafts in cell membranes. *Nature* **387**, 569–572 (1997).
75. Pike, L. J. & Casey, L. Cholesterol Levels Modulate EGF Receptor-Mediated Signaling by Altering Receptor Function and Trafficking. *Biochemistry* **41**, 10315–10322 (2002).
76. Zhang, G. et al. CD317 Activates EGFR by Regulating Its Association with Lipid Rafts. *Cancer Res.* **79**, 2220–2231 (2019).
77. Coskun, U., Grzybek, M., Drechsel, D. & Simons, K. Regulation of human EGF receptor by lipids. *Proc. Natl. Acad. Sci. USA* **108**, 9044–9048 (2011).
78. Irwin, M. E., Mueller, K. L., Bohin, N., Ge, Y. & Boerner, J. L. Lipid raft localization of EGFR alters the response of cancer cells to the EGFR tyrosine kinase inhibitor gefitinib. *J. Cell Physiol.* **226**, 2316–2328 (2011).
79. Nair, A., Chauhan, P., Saha, B. & Kubatzky, K. F. Conceptual Evolution of Cell Signaling. *Int. J. Mol. Sci.* **20** (2019).
80. Sainz-Mejias, M., Jurado-Martin, I. & McClean, S. Understanding *Pseudomonas aeruginosa*-Host Interactions: The Ongoing Quest for an Efficacious Vaccine. *Cells* **9** (2020).
81. Frimmersdorf, E., Horatzek, S., Pelnikovich, A., Wiehlmann, L. & Schomburg, D. How *Pseudomonas aeruginosa* adapts to various environments: a metabolomic approach. *Environ. Microbiol.* **12**, 1734–1747 (2010).
82. Palmer, K. L., Aye, L. M. & Whiteley, M. Nutritional cues control *Pseudomonas aeruginosa* multicellular behavior in cystic fibrosis sputum. *J. Bacteriol.* **189**, 8079–8087 (2007).
83. Chang, Y. et al. Usage of density analysis based on micro-CT for studying lung injury associated with burn-blast combined injury. *Burns* **44**, 905–916 (2018).
84. Bai, X. et al. Structure and dynamics of the EGFR/HER2 heterodimer. *Cell Discov.* **9** (2023).
85. Ershov, D. et al. TrackMate 7: integrating state-of-the-art segmentation algorithms into tracking pipelines. *Nat. Methods* **19**, 829–832 (2022).
86. Vega, A. R., Freeman, S. A., Grinstein, S. & Jaqaman, K. Multistep track segmentation and motion classification for transient mobility analysis. *Biophys. J.* **114**, 1018–1025 (2018).
87. Qin, G., Xu, J., Liang, Y. & Fang, X. Single-molecule imaging reveals differential AT1R Stoichiometry change in biased signaling. *Int. J. Mol. Sci.* **25**, 374 (2024).
88. Qin, G. et al. A signaling molecule from intratumor bacteria promotes trastuzumab resistance in breast cancer cells. *Proc. Natl. Acad. Sci.* **122**, e2421710122 (2025).

89. Simons, K. & Ikonen, E. Functional rafts in cell membranes. *Nature* **387**, 569–72 (1997).
90. Risselada, H. J. & Marrink, S. J. The molecular face of lipid rafts in model membranes. *Proc. Natl. Acad. Sci. USA* **105**, 17367–72 (2008).
91. Poruthoor, A. J., Sharma, A. & Grossfield, A. Understanding the free-energy landscape of phase separation in lipid bilayers using molecular dynamics. *Biophys. J.* **122**, 4144–4159 (2023).
92. Ogiso, H. et al. Crystal structure of the complex of human epidermal growth factor and receptor extracellular domains. *Cell* **110**, 775–787 (2002).
93. Jo, S., Kim, T., Iyer, V. G. & Im, W. CHARMM-GUI: A web-based graphical user interface for CHARMM. *J. Comput. Chem.* **29**, 1859–1865 (2008).
94. Jeffery B. et al. Update of the CHARMM All-Atom Additive Force Field for Lipids: Validation on Six Lipid Types. (2010).
95. Abraham, M. J. et al. GROMACS: High performance molecular simulations through multi-level parallelism from laptops to super-computers. *SoftwareX* **1–2**, 19–25 (2015).
96. Lee, J. et al. CHARMM-GUI Input Generator for NAMD, Gromacs, Amber, Openmm, and CHARMM/OpenMM Simulations using the CHARMM36 Additive Force Field. *Biophys. J.* **110**(2016).
97. Marrink, S. J., Risselada, H. J., Yefimov, S., Tieleman, D. P. & De Vries, A. H. The MARTINI Force Field: Coarse Grained Model for Biomolecular Simulations. *J. Phys. Chem. B* **111**, 7812–7824 (2007).
98. Nosé, S. A unified formulation of the constant temperature molecular dynamics methods. *J. Chem. Phys.* **81**, 511–519 (1984).
- Z.Z. and D.Z. helped with the animal's experiments. H.R. and T.X. helped molecular imaging experiment. Y.S. and T.Y. were responsible for the overall design and wrote the manuscript.

Competing interests

Y.S. is a shareholder of Benethera Biotechnologies. The remaining authors declare no competing interests.

Additional information

Supplementary information The online version contains supplementary material available at <https://doi.org/10.1038/s41467-025-66989-x>.

Correspondence and requests for materials should be addressed to Tongtao Yue or Yan Shi.

Peer review information *Nature Communications* thanks the anonymous reviewers for their contribution to the peer review of this work. A peer review file is available.

Reprints and permissions information is available at <http://www.nature.com/reprints>

Publisher's note Springer Nature remains neutral with regard to jurisdictional claims in published maps and institutional affiliations.

Open Access This article is licensed under a Creative Commons Attribution-NonCommercial-NoDerivatives 4.0 International License, which permits any non-commercial use, sharing, distribution and reproduction in any medium or format, as long as you give appropriate credit to the original author(s) and the source, provide a link to the Creative Commons licence, and indicate if you modified the licensed material. You do not have permission under this licence to share adapted material derived from this article or parts of it. The images or other third party material in this article are included in the article's Creative Commons licence, unless indicated otherwise in a credit line to the material. If material is not included in the article's Creative Commons licence and your intended use is not permitted by statutory regulation or exceeds the permitted use, you will need to obtain permission directly from the copyright holder. To view a copy of this licence, visit <http://creativecommons.org/licenses/by-nc-nd/4.0/>.

© The Author(s) 2025

Acknowledgements

We thank Dr Xiaoyu Hu of Tsinghua University for providing *stat3^{fl/fl}* mice, Dr Kangmin He of Institute of Genetics and Developmental Biology, Chinese Academy of Sciences for EGFR-Halo knock-in Genome-edited HEK293. Hefei Ruan is supported by National Natural Science Foundation of China (32000873). YS is supported by the joint Peking-Tsinghua Center for Life Sciences, the National Key R&D Program of China (2023YFC2306300), the National Natural Science Foundation of China General Program (31370878), State Key Program (31630023) and Innovative Research Group Program (81621002). TY is supported by National Natural Science Foundation of China (32371459) and Natural Science Foundation of Shandong Province (ZR2021YQ23).

Author contributions

M.Z. performed the cell and the animal experiments and analyzed the data. J.C. performed all-atom molecular dynamics experiments. G.Q. performed single molecule tracking and photobleaching experiment.